MASTER

Instationary flow in a straight, distensible tube : analysis of wall and fluid motion

Westenberg, J.J.M.

Award date:
1993

Link to publication

Instationary flow in a straight, distensible tube: analysis of wall and fluid motion

J.J.M. Westenberg, juli 1993
R-1228-A / WFW 93-099

Begeleiding :   Dr. Ir P.H.M. Bovendeerd
Afstudeerdocenten :   Dr. Ir. M.E.H. van Dongen
                           Prof. Dr. Ir. J.D. Janssen

Abstract

Wall and fluid behaviour in arteries are investigated in order to obtain information about the genesis of atherosclerosis, an arterial disease. The carotid artery bifurcation is often involved in the atherosclerotic process, leading to cerebral vascular disease. Reuderink (1991) developed a numerical method for simulation of the flow through and the deformation of a distensible model of the carotid artery bifurcation. This numerical method has to be validated experimentally.

To make this validation in the future possible an experimental method for the measurement of the deformation of a simplified model is presented here. A straight, distensible tube is used to model the communis, the main branch of the carotid artery bifurcation. The instationary flow through the communis is modelled by a harmonical varying flow. The deformation of the tube is determined via optical registration of the movement of markers on the outside of the tube wall. Radial and axial expansion, translation and rotation of the tube are measured, along with flow parameters like the transmural pressure, the axial velocity profile and the flow. The Reynolds number is set to vary harmonically between 200 and 800 and the Womersley parameter is 4.9. These parameters are in the same range as in the physiological situation.

The measured radial expansion varies harmonical between 6% and 14%, while no axial expansion is found. Also a small rotation of the tube occurs (about 1°) which varies harmonical with an amplitude of 1° and the tube is translated lateral during the deformation. The flow and the transmural pressure occur as standing waveforms.

The measured axial velocity profile is compared to two theoretical profiles. First an analytical profile is determined from Womersley's rigid tube theory. Secondly, the measured wall movement is taken into account in a numerical model. The axial velocity profile determined from this numerical model seems to be an improvement over the analytical profile. This numerical profile and matching wall shear rate show better agreement with the experimentally determined profile and wall shear rate.

List of used symbols

A	cross-sectional area
c	Moens-Korteweg wave velocity
C_1, C_2	complex functions, in the amplitude of the pressure
E	modulus of elasticity
e	constant number ($e \approx 2.718281828$)
$\vec{e}_r$	radial unit vector
$\vec{e}_x$	unit vector in x direction
$\vec{e}_y$	unit vector in y direction
$\vec{e}_z$	axial unit vector
f	source term ($f(\tau) = -\dfrac{T}{\rho V}\dfrac{\partial P}{\partial z}(\tau)$)
h	wall thickness
i	imaginary number
J_0	Besselfunction of the first kind of order 0
J_1	Besselfunction of the first kind of order 1
k	propagation coefficient
L	characteristic length
l	tube length
L_e	entrance length
m	spatial discretization
n	time discretization
O	order
P	local pressure
p	instationary part of the pressure
p_{stat}	stationary part of the pressure
p_0	amplitude of the instationary part of the pressure
Q	flow
Q_{exp}	experimental flow
Q_{in}	ingoing flow
Q_{mean}	mean of the flow
Q_{model}	model flow
Q_{out}	outgoing flow
$Q_{storage}$	storage flow
Q_1	first harmonic of the flow
R	inner radius
$\hat{R}$	amplitude inner radius
R_0	inner radius in reference state
$\Re$	real part of a complex number
Re	Reynolds number
r	radial coordinate
r_0	radial position in reference state
t	time
T	cyclus time
$\vec{r}$	translation vector
u	radial fluid velocity

u_l	lateral translation
u_z	axial translation
$u_\perp$	perpendicular translation
V	characteristic velocity
$\vec{v}$	velocity
V_1, V_2	velocities
w	axial velocity
w_p	stationary part of the radial velocity
w_l	amplitude of the instationary part of the radial velocity
$\bar{w}$	mean axial velocity
$\hat{w}$	dimensionless axial velocity ($\hat{w} = w/V$)
$\vec{x}$	position vector
$\vec{x}_0$	position vector in reference state
y	dimensionless transformation coordinate ($= r/R_0$)
z	axial coordinate
z_0	axial position in reference state

α	Womersley parameter
Γ	reflection coefficient
Δ	discretization
ε	error through projection
ε_2	error
η	dynamic viscosity
λ	wave length
λ_r	radial expansion
λ_z	axial expansion
ν	kinematic viscosity
ξ	dimensionless transformation coordinate ($\xi = r/R(t)$)
π	constant number ($\pi \approx 3.141592654$)
ρ	specific gravity
σ	standard deviation
τ	dimensionless time ($\tau = t/T$)
ϕ	circumferential coordinate
ϕ_R	phase inner radius movement
ϕ_{rot}	rotation angle
ϕ_0	circumferential position in reference state
χ	convective term ($\chi(\xi,\tau) = -\dfrac{\nu T}{R^2(\tau)} + \dfrac{\xi^2}{R(\tau)}\dfrac{dR(\tau)}{d\tau}$)
ψ	diffusion term ($\psi(\tau) = \dfrac{\nu T}{R^2(\tau)}$)
ω	angular frequency
∇	gradient

Contents

4

1 Introduction

Atherosclerosis is an arterial disease which may lead to narrowing (stenosis) of the artery. Stenoses are preferably found in arterial bends and bifurcations. The carotid artery bifurcation is often involved in the atherosclerotic process, leading to cerebral vascular disease. In figure 1.1 the mean geometry of the carotid artery bifurcation is given. The geometry parameters are obtained from Bharadvaj (1982).
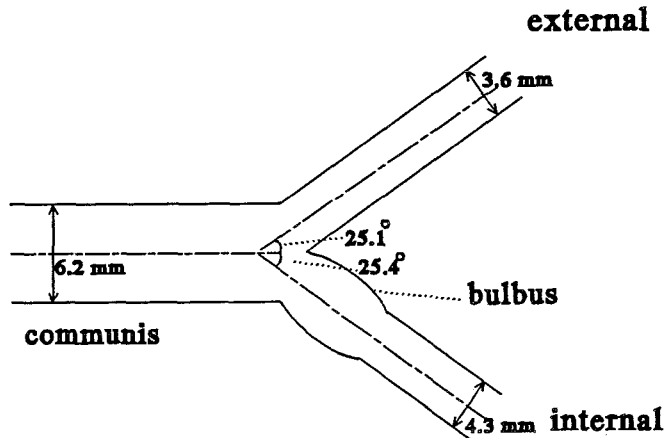

figure 1.1: sketch of the human carotid bifurcation.

The carotid artery bifurcation consists of a main branch (the communis) which divides into two branches. The internal carotid artery passes blood through to the brain, the external carotid artery provides the face with blood. A stenosis is most likely to occur in the bulbus. In this section secundairy flow occurs and locally the blood velocity can be low. Even backflow can occur in this section.

The University of Limburg and the Eindhoven University of Technology cooporate in the "Atherosclerose"-project. Main goal of this project is early detection and better diagnostic treatment of atherosclerosis. To achieve this, better insight in the genesis of a stenosis and in the flow in the carotid artery bifurcation is needed, along with the study of the movement of the arterial wall.

Reuderink (1991) developed a numerical method for simulation of the flow through and the deformation of a distensible model of the carotid artery bifurcation. He solved the equations for fluid flow and wall movement in an uncoupled way. This method has to be validated experimentally. Part of this validation is the measurement of the time-dependent deformation of a distensible model of the carotid artery bifurcation.

To make this measurement in the future possible an experimental method for measurement of the deformation of a simplified model (a uniform distensible, straight tube with an isotropic, linearly elastic wall) is presented here. This method is based upon optical registration of the movement of markers, which are placed on the outside of the wall of the tube. The movement of the markers due to an instationary flow through the tube is analysed with image processing techniques and from this movement the deformation of the tube is calculated. This deformation is coupled to flow parameters like the

5

transmural pressure, flow and velocity. In chapter 2 the experimental setup and the method for the deformation measurement is presented.

For the prediction of the fluid velocity both an analytical and a numerical model are used. Womersley (1957) presented an analytical model for the prediction of the velocity field in a straight, rigid tube due to a harmonically varying pressure gradient. Dutta and Tarbell (1989) took the wall motion into account by a different treatment of the boundary conditions. In this way a numerical approach has to be used. In chapter 2 both the analytical model based on Womersley's theory and the numerical model based on Dutta and Tarbell's theory are explained.

In chapter 3 the results, both from the experiments and from the theoretical models, are presented. These results are discussed and compared with each other in chapter 4. In this chapter the physiological application of the results is also given. Finally, in chapter 5 the conclusions together with suggestions for future work are given.

2 Material and methods

2.1 Physiological flow in the human communis

The oscillatory flow of an incompressible fluid in general can be characterized by two dimensionless parameters, the Womersley parameter $\alpha = R\sqrt{\omega/\nu}$ and the Reynolds number $Re = LV/\nu$, where R is the tube inner radius, ω de angular frequency, ν the kinematic viscosity, L a characteristic length (= the tube inner diameter) and V a characteristic velocity (= the mean axial fluid velocity) (Paterson (1983)). The Womersley parameter gives the ratio between the instationary and the viscous forces in the flow equations and the Reynolds number gives the ratio between the stationary and the viscous forces. The inner radius of the communis is 3.1 mm (all physiological parameters are taken from Balsubramanian (1979)). Blood is assumed to behave like an incompressible Newtonian fluid. For the kinematic viscosity of blood is $\nu = 3.5 \cdot 10^{-6}$ m²/s assumed, while the specific gravity ρ of blood amounts to $1.06 \cdot 10^3$ kg/m³. During one hartcylce the Reynolds number in the communis varies between 175 and 650. With a frequency of 1 Hz the Womersley parameter will be equal to 4.2.

The arterial wall is anisotropic and behaves viscoelastic. The thickness of the wall of the communis is 0.4 mm. The length of the communis equals about 15 cm. The specific gravity of the wall amounts to $1.05 \cdot 10^3$ kg/m³. E, the modulus of elasticity, equals $4.5 \cdot 10^5$ N/m², the wave velocity $c = 5.0$ m/s (experimentally determined (Pedley (1980)) and the wave length $\lambda = 5.0$ m. During one hartcycle the communis expands 10% radially.

2.2 The experimental model

2.2.1 The experimental setup

In this study the geometry of the carotid artery bifurcation has been greatly simplified to the geometry of a distensible, straight tube. The physiological situation has to be taken into account for the scaling of the experimental model.

Fluid velocity inside the tube is measured using laser Doppler anemometry (LDA). This implies that the material from which the tube is manufactured, has to be transparent.

The tube is made of two component silicon rubber Sylgard 184 (Dow Corning). In a mould a distensible tube has been made. The accuracy of the dimensions of the tube are assumed to be the same as the accuracy of the dimensions of the mould. This way the tube has a length of 510.00 ± 0.01 mm, an inner radius of 9.00 ± 0.01 mm and a wall thickness of 1.00 ± 0.01 mm (Rutten (1993)). In figure 2.1 the tube is sketched.

The index of refraction of the tube is 1.4110 ± 0.0002. Through the tube a solution of 30% CaCl₂ in water flows. The index of refraction of the solution has to be matched to the index of refraction of the tube, so there will be no refraction of the laserbeam at the tube wall. This can be done with a maximal deviation of 0.2%. The index of refraction of the solution can be controlled by adjusting the concentration of the
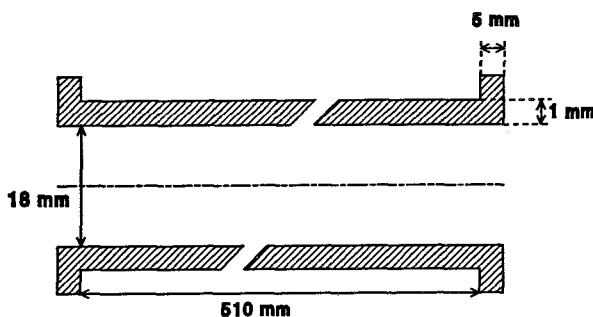
figure 2.1: the tube.

solution. The dynamic viscosity η of the solution is $(3.10 \pm 0.02) \cdot 10^{-3}$ kg/ms and the specific gravity ρ ammounts to 1262 ± 15 kg/m^3. For the detection of the velocity with LDA seeding (0.5 cc oil/l fluid) is added to the solution.

The tube is stretched in a rectangular perspex reservoir which is filled with the same solution as is used inside the tube. The axial pre-strain of the tube is 10%. This way the inner radius will become 8.73 ± 0.01 mm. The effective free moving length of the tube becomes 500.00 ± 0.5 mm (the accuracy is based on the dimensions of the reservoir). The modulus of elasticity E of the tube wall is experimentally found to be $(0.99 \pm 0.03) \cdot 10^6$ N/m^2 (Appendix B). The specific gravity of the wall is 1050 ± 5 kg/m^3 (specifications Dow Corning for Sylgard 184 at 25° C).

An instationary, harmonically varying flow is created through the tube. The flow parameters are set to the same range of those in the physiological situation. The angular frequency is set to 0.786 ± 0.001 rad/s. This way the Womersley parameter is 4.9 ± 0.1. The Reynolds number varies harmonically between 200 ($\pm$ 23) and 800 ($\pm$ 29). The Moens-Korteweg wave velocity is determined from

$$ c = \sqrt{\frac{hE}{2R\rho}} \qquad (2.1) $$

where h is the wall thickness. In the experiments the Moens-Korteweg wave velocity becomes 6.7 ± 0.3 m/s and the wave length becomes 54 ± 2 m. In table 1 the comparison between the physiological situation and the experimental model is given.

	physiological situation	experimental model
Reynolds number	175 - 650	200 ($\pm$ 23) - 800 ($\pm$ 29)
Womersley parameter	4.2	4.9 ± 0.1
angular frequency	6.28 rad/s	0.786 ± 0.001 rad/s
kinematic viscosity	$3.5 \cdot 10^{-6}$ m^2/s	$(2.46 \pm 0.05) \cdot 10^{-6}$ m^2/s
specific gravity fluid	1060 kg/m^3	1262 ± 15 kg/m^3
specific gravity wall	1050 kg/m^3	1050 ± 5 kg/m^3
wall thickness	0.4 mm	1.00 ± 0.01 mm
inner radius	3.1 mm	8.73 ± 0.01 mm
tube length	150 mm	500.00 ± 0.5 mm
M.K. wave velocity	5.0 m/s	6.7 ± 0.3 m/s
wave length	5.0 m	54 ± 2 m
tube length : wave length	$2.9 \cdot 10^{-2}$	$0.9 \cdot 10^{-2}$
inner radius : wave length	$6.0 \cdot 10^{-4}$	$1.6 \cdot 10^{-4}$

Table 1: scaling experimental model to physiological situation.

The tube is installed in a closed flowcircuit which is sketched in figure 2.2.
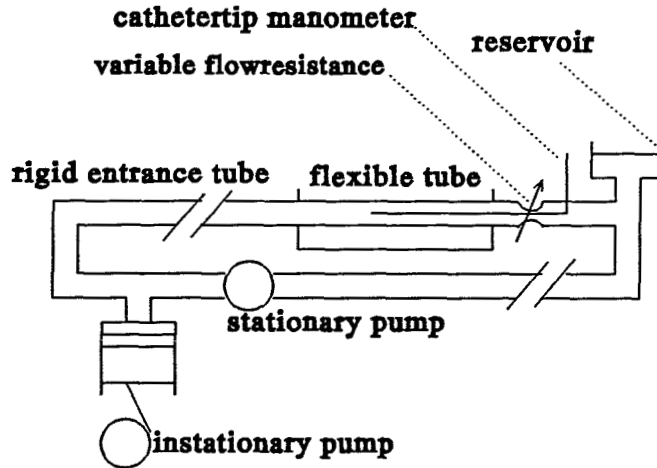

fig 2.2: the flowcircuit.

A stationary pump leads the fluid from a reservoir to the distensible tube via a rigid entrance tube with a length of 3.75 m. For the development of the axial velocity profile in a cylindrical tube a minimal entrance length L_e is needed (Vossers (1986)). When a stationary plane velocity profile enters the tube, the entrance length is given by

$$L_e = 0.056 \times Re \times 2R \tag{2.2}$$

This way, for $Re = 800$, the minimal entrance length becomes 0.8 m. The assumption that the instationary axial velocity profile will be fully developed is a safe one, because the minimal entrance length for an instationary flow is generally *shorter* than the minimal entrance length for a stationary flow.

The stationary flow is set to a constant amount so that the Reynolds number for this stationary flow is 500. For the characteristic velocity the mean axial velocity $\bar{w}$ is taken. This follows from

$$\bar{w} = \frac{Q}{\pi R^2} \tag{2.3}$$

with Q the flow.

Between the stationary pump and the entrance tube an instationary pump is installed. This pump generates an instationary flow which varies sinusoidally. This instationary flow is superposed to the stationary flow. The total Reynolds number varies harmonically between 200 and 800 with the total instationary flow remaining positive.

The transmural pressure across the tube can be set with a variable flowresistance at the distal end of the tube. This way a radial expansion of 10% can be obtained. The radial expansion in the experimental model is in the same range as the radial expansion in the communis.

2.2.2 Measurement of fluid behaviour

The following flow quantities are experimentally determined on three axial positions:

- the local velocity profile,
- the local transmural pressure,
- the flow proximally and distally from the distensible tube.

The local velocity is measured with laser Doppler anemometry (LDA). With LDA a laserbeam is scattered by moving particles inside the fluid and this causes a Doppler shift for the frequency of the light of the laserbeam. From this Doppler shift the local fluid velocity can be determined. The velocity is measured with an accuracy of 3 mm/s.

From the local velocity profile the local flow and the wall shear rate are determined. The local flow is obtained by integrating the profile over the tube cross-section. The wall shear rate is approximated by calculating the finite difference quotient of the velocity profile near the wall.

The local pressure inside the tube is determined with a cathetertip manometer (Millar) which can be placed at an arbitrary position. The local pressure is determined with regard to the pressure when there is no flow (in this situation the pressure inside the tube will be equal to the pressure outside the tube). This way the cathetertip manometer measures the transmural pressure. The accuracy for pressure measurement is 0.1 kPa.

The flow is determined at two positions with two electro-magnetic flowmeters (Scalar Medical). The first one is positioned at approximately 5 m proximally from the distensible tube, the second one approximately 20 cm distally from the tube. The accuracy for flow measurement is 20 ml/min.

2.2.3 Measurement of wall behaviour

A set of twenty markers (inkspots with a diameter of approximately 1 mm) are placed on the upperside of a segment of the tube on the outside wall. These twenty markers are placed on four virtual lines with a length of 32 mm parallel to the tube axis. Together with four calibration markers, which are placed in a square on fixed distances (35 mm) beside the tube, this segment with markers is filmed with a camera which is placed 400 mm above the tube. A second camera films a timer which is triggered by the LDA measurement unit. This timer takes care of the synchronisation between the deformation measurement and the LDA velocity measurement. The image of the second camera is mixed together with the image of the tube. In figure 2.3 the tube together with the calibration markers and the total camera image are sketched.
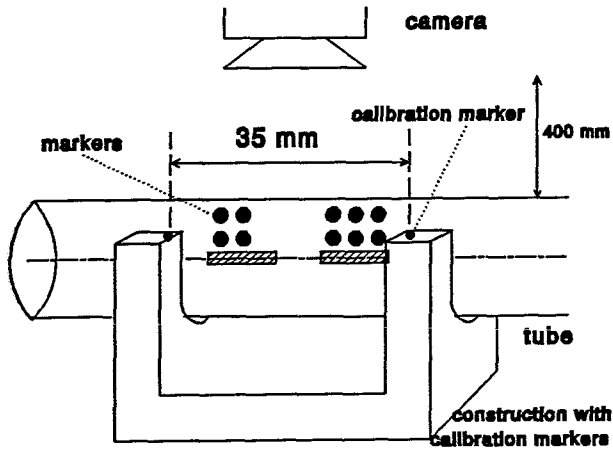
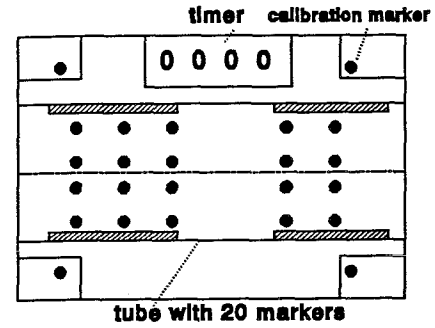*fig 2.3 a: tube with the calibration markers.*　　　　*fig 2.3 b: video image.*

The used axisframe is sketched in figure 2.4.

　　The transformation of a point on the tube wall, which is represented by the vector $\vec{x}_0 = r_0\vec{e}_r + z_0\vec{e}_z$, from the reference state when there is no flow through the tube, to a deformated state can be divided into the following linear transformations. First the tube expands radially and axially. This expansion is given by

figure 2.4: axisframe.

$$r = \lambda_r r_0$$
$$z = \lambda_z z_0$$

(2.4)

with λ_r and λ_z the expansion in radial r and axial z direction, respectively. Secondly, the tube rotates along the tube axis with rotation angle ϕ_{rot}. Next the vector becomes translated in the image-plane, prescribed by the translation vector $\vec{t} = u_l\vec{e}_x + u_\perp\vec{e}_y + u_z\vec{e}_z$ where u_l, $u_\perp$ and u_z are the lateral, perpendicular (to the image plane) and axial translation of the tube. Finally, the vector is projected on the image plane, which is spanned by $\vec{e}_x$ en $\vec{e}_z$. The position of a vector on the tube wall in the deformated state can be given by

$$\vec{x} = (\lambda_r r_0 \cos(\phi_0 + \phi_{rot}) + u_l)\vec{e}_x + (\lambda_z z_0 + u_z)\vec{e}_z$$

(2.5)

　　In the reference state the circumferential position of each marker is determined. When the tube undergoes a deformation caused by an instationary flow through the tube, the markers will move correspondingly. Under the assumption that the radial expansion is independent of the circumferential position (this means that the tube must be circumferentially homogeneous), the rotation, radial and axial expansion and lateral and axial translation of a segment of the tube can be determined as function of the time. This is done using the following procedure.

　　The movement of the markers during one flowcycle is filmed and recorded on videotape. From the videoimages the position of each marker is obtained with the TIM

11

image processing software (Difa). From the movement of the whole set of markers with respect of the reference (no flow) state, which is recorded and analysed too, a radial and axial expansion is determined for each marker. The markers are placed on four virtual lines parallel to the tube axis (see figure 2.3 b). Without accounting for rotation of the tube along its axis the radial expansion seemed to depend on the circumferential position of the marker (Appendix A). Markers on a line which was nearer to the right-hand side of the tube (when viewed in the flow direction) seemed to expand more than markers on other lines. With the above mentioned assumption that the tube was circumferentially homogeneous, this marker motion can only be described with a combined radial expansion and rotation of the segment.

From the movement of the coordinates of the markers radial and axial expansion are determined for each marker. The expansion is determined from the two dimensional Green-Lagrange strain field, which is determined with software from C. Oomens. The lateral and axial translation (these follow from the centre point movement of the markers) for the whole segment are determined too. Then the residu of the radial expansion of each marker is determined. The coordinates of each marker are adapted for a value of the rotation angle of the whole segment and again expansion and translation are determined. The value of the rotation angle for which a minimal residu is calculated, is iteratively determined. The matching values for radial and axial expansion and lateral and axial translation are now the true values for the deformation of the segment. The mean value of the standard deviation for the radial and axial expansion is 0.007. This is deducted from the minimal residu. The mean standard deviation for the translation, laterally and axially, is 0.04 mm. This follows from the standard deviation for the determination of the coordinates of the markers, which equals to 0.2 pixel. The maximal error in the rotation angle is 0.3° (based on the accuracy for the determination of the coordinates of a marker). This is quit big, but rotation correction is, as proved in Appendix A, relevant.

2.2.4 Experimental protocol

Wall and fluid behaviour are investigated at three segments (125 mm apart) of the tube which are referred to as segment 000, 125 and 250. For these segments the restrainted ends of the tube (where the tube is attached to the reservoir) have no effect on the expansion anymore (see Appendix B). The position of each segment is sketched in figure 2.5.

The following protocol is used for flow - deformation measurement at each segment. First the situation with no flow through the tube is filmed. The coordinates of the markers define the reference state of the tube for the deformation

figure 2.5: segments for deformation detection.

measurement. At the same time the outer diameter is measured using the laser. The laser is traversed until the beam just strikes the outer wall on the upperside of the tube. Traver-
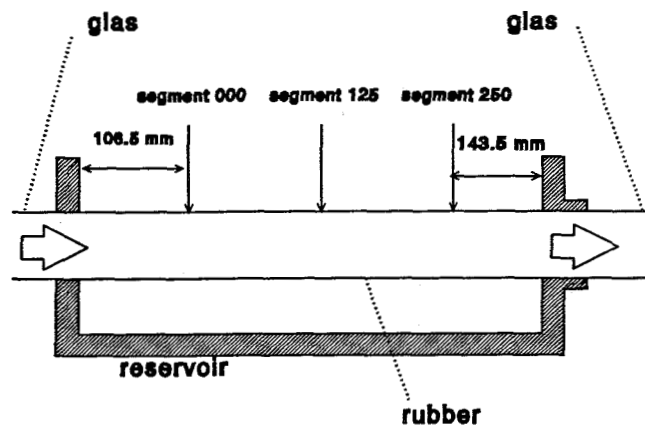
sing in vertical direction to the other outer wall yields the outer diameter. Then the instationary flow through the tube is generated and the motion of the markers is recorded during a few cycles. One cycle is used to determine the deformation parameters. During this cycle 25 images are processed, leading to radial and axial expansion, rotation and lateral and axial translation. From the radial expansion the local inner radius is calculated, with the assumption that the tube material is incompressible.

After the deformation measurement the fluid behaviour is determined (Rutten (1993)). The flows proximally and distally from the tube are measured. At every segment fluid velocity and transmural pressure are determined.

As already mentioned, the velocity is measured using LDA. Fluid velocities are measured at 62 sample points in the cross-section (see figure 2.6).
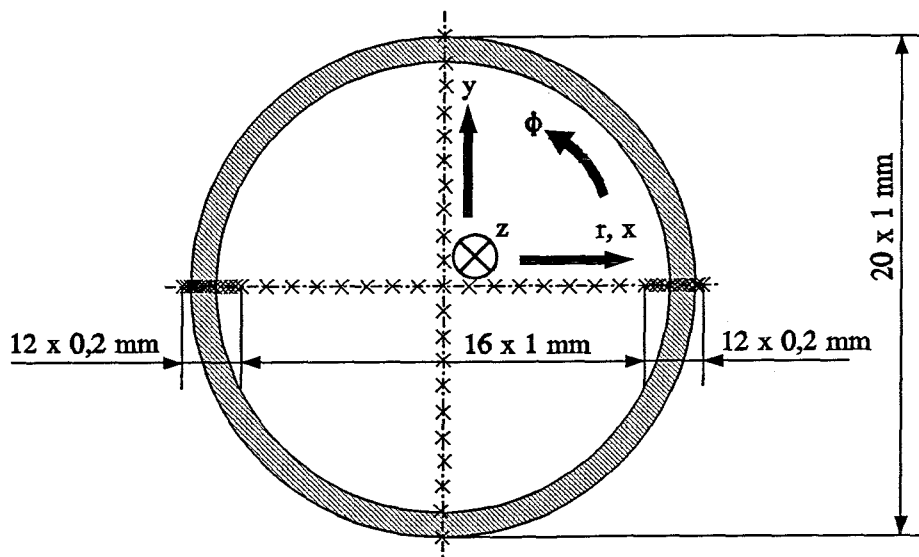

figure 2.6: positions velocity sample points in cross-section. (from Rutten (1993))

All measurements of the parameters related to the fluid behaviour are carried out during 25 cycles and these are averaged.

2.3 The analytical model

In the experimental setup a variable resistance is placed at the distal end of the distensible tube for controlling the pressure inside the tube. This resistance is a sudden cross-section narrowing. A pressure wave through the tube is reflected at this resistance with a reflection coefficient $\Gamma \approx 1$. The local pressure inside the tube can be observed as a superposition of an incident and a reflected wave on a stationary value:

$$P(z) = p_{stat}(z) + p(z) = p_{stat}(z) + \Re[p_0 e^{i(\omega t - kz)} + \Gamma p_0 e^{i(\omega t + k(z - l))}] \qquad (2.6)$$

with k the propagation coefficient ($\approx 0.1 \text{ m}^{-1}$) and l the tube length. For convenience we will take the phase of p_0 equal to zero, so that p_0 is synonymous to the pressure amplitude of the instationary component at the entrance $z = 0$. The expansion of the instationary part

13

of the local pressure becomes

$$p(z) = \Re(p_0 e^{i\omega t} [1 + \Gamma \{1 - ikl + \frac{(ikl)^2}{2!} + O(k^3)\} + ikz(-1 + \Gamma\{1 - ikl + O(k^2)\}) +$$

$$+ \frac{(ikz)^2}{2!} (1 + \Gamma \{1 + O(k)\}) + O(z^3 k^3)]) \tag{2.7}$$

and the axial component of the pressure gradient becomes

$$\frac{\partial p}{\partial z} = \Re(p_0 e^{i\omega t} [ik \{-1 + \Gamma (1 - ikl + O(k^2))\} + \tag{2.8}$$

$$+ (ik)^2 z \{1 + \Gamma (1 + O(k))\} + O(z^2 k^3)])$$

In the case of a wave with a long wavelength and a reflectioncoefficient approximately 1, (2.7) and (2.8) become

$$p(z) = \Re(\{C_1 + C_2(kz)\}e^{i\omega t}) \tag{2.9}$$

$$\frac{\partial p}{\partial z} = \Re(C_2 e^{i\omega t}) \tag{2.10}$$

with C_1 and C_2 complex functions. The wave character inside the tube can be described by a standing waveform.

Now we analyse the local fluid behaviour. Generally, the flow of an incompressible fluid is prescibed by the Navier-Stokes equation and the equation of continuity:

$$\frac{\partial \vec{v}}{\partial t} + (\vec{v}.\nabla)\vec{v} = -\frac{1}{\rho}\nabla P + \nu\nabla^2\vec{v} \tag{2.11}$$

$$\nabla\cdot\vec{v} = 0 \tag{2.12}$$

with $\vec{v}$ the fluid velocity and t the time. For an axi-symmetric geometry cylindrical coordinates can be used. If the tube diameter is much smaller than the tube length, the radial velocity component u will be zero and the axial velocity w will be fully developed ($(\vec{v}.\nabla)\vec{v} = 0$ in (2.11)). The equation of motion becomes

$$\frac{\partial w}{\partial t} = -\frac{1}{\rho}\frac{\partial P}{\partial z} + \nu(\frac{\partial^2 w}{\partial r^2} + \frac{1}{r}\frac{\partial w}{\partial r}) \tag{2.13}$$

with r and z the radial and axial coordinate.

Womersley (1957) solved the equation of motion (2.13) for a rigid tube with a harmonical pressure gradient as in (2.10). He used the transformation $y = r/R_0$ and by substitution of a harmonical solution $w = w_1(r)e^{i\omega t}$ for the axial velocity he found the following partial differential equation:

14

$$\frac{\partial^2 w_1(y)}{\partial y^2} + \frac{1}{y}\frac{\partial w_1(y)}{\partial y} + i^3\alpha^2 w_1(y) = C\frac{R_0^2}{\eta} \tag{2.14}$$

For a rigid tube a homogeneous Dirichlet boundary condition (no slip) has to be used:

$$w_1(1) = 0 \tag{2.15}$$

This yields the following analytical solution of the axial velocity profile:

$$w(y,t) = \Re(-\frac{C}{i\omega\rho}\{1 - \frac{J_0(\alpha i^{3/2}y)}{J_0(\alpha i^{3/2})}\}e^{i\omega t}) \tag{2.16}$$

with J_0 the Besselfunction of the first kind of order 0.

This solution is used as a first estimate for the local axial velocity profile at position 000 in the distensible tube. Womersley used the pressure gradient as input parameter for his model. With the used experimental setup it is not possible to measure the axial pressure gradient. The cathetertip manometer has an accuracy of 0.1 kPa. With a tube length of 500 mm only pressure gradients with values higher than 0.2 kPa/m can be significantely determined. Instead of the gradient the mean and first harmonic of both the local flow and the inner radius are used as input parameters. From the inner radius the cross-sectional area is obtained. The local flow is obtained with by integrating the experimentally determined (discrete) velocity profile with the use of the trapezium-rule over the cross-section.

With the cross-sectional area and the mean of the flow the quasi-stationary velocity (Poiseuile) profile can be obtained by

$$w_P(y,t) = 2\frac{Q_{mean}}{A(t)}(1 - y)^2 \tag{2.17}$$

With (2.16) and the use of the cross-sectional area and the first harmonic of the flow Q_1 the first harmonic of the axial velocity profile can be obtained by

$$w_1(y,t) = \Re(\frac{Q_1(t)}{A(t)}\frac{1 - \dfrac{J_0(\alpha i^{3/2}y)}{J_0(\alpha i^{3/2})}}{1 - \dfrac{2J_1(\alpha i^{3/2})}{\alpha i^{3/2}J_0(\alpha i^{3/2})}}) \tag{2.18}$$

with J_1 the Besselfunction of the first kind of order 1. Because of the linearity the total axial velocity profile predicted by Womersley's theory is the summation of (2.17) and (2.18).

The profile is axi-symmetric. The variable y is multiplied with the experimentally determined inner radius, which is time-dependent, to account for the wall motion.

15

2.4 The numerical model

Dutta and Tarbell (1989) presented a different procedure for the solution of the axial component of the Navier-Stokes equation. They took into account the wall motion directly in the radial coordinate transformation $\xi(t) = r/R(t)$. With this transformation the axial component of the Navier-Stokes equation becomes (see Appendix C)

$$
\frac{\partial w}{\partial t} - \frac{\xi}{R}\frac{\partial w}{\partial \xi}\frac{\partial R}{\partial t} + \frac{u}{R}\frac{\partial w}{\partial \xi} + w[-\frac{\xi}{R}\frac{\partial w}{\partial \xi}\frac{\partial R}{\partial z} + \frac{\partial w}{\partial z}] =
$$
$$
= -\frac{1}{\rho}\frac{\partial P}{\partial z} + \nu\{\frac{1}{R^2}\frac{\partial^2 w}{\partial \xi^2} + \frac{1}{\xi R^2}\frac{\partial w}{\partial \xi} + \frac{\partial^2 w}{\partial z^2} + \frac{\partial w}{\partial \xi}[\frac{2\xi}{R^2}(\frac{\partial R}{\partial z})^2 + \qquad (2.19)
$$
$$
- \frac{\xi}{R}\frac{\partial^2 R}{\partial z^2}] + \frac{\partial^2 w}{\partial \xi^2}(-\frac{\xi}{R}\frac{\partial R}{\partial z})^2 + \frac{\partial w}{\partial \xi}(-\frac{1}{R}\frac{\partial R}{\partial z})(-\frac{\xi}{R}\frac{\partial R}{\partial z}) + \frac{\partial^2 w}{\partial \xi \partial z}(-\frac{\xi}{R}\frac{\partial R}{\partial z})\}
$$

After estimating the value of all terms and taking only the relevant terms into account, (2.19) becomes (see also Appendix C) after some rewriting

$$
\frac{\partial w}{\partial t} = \nu[\frac{1}{R^2(t)}\frac{\partial^2 w}{\partial \xi^2} + \frac{1}{\xi R^2(t)}\frac{\partial w}{\partial \xi}] - \frac{1}{\rho}\frac{\partial P}{\partial z}(t) + \frac{\xi}{R(t)}\frac{dR(t)}{dt}\frac{\partial w}{\partial \xi} \qquad (2.20)
$$

Symmetry and no slip conditions are taken into account by homogeneous Neumann and Dirichlet boundary conditions:

$$
\frac{\partial w}{\partial \xi} = 0 \quad , \quad \xi = 0
$$
$$
w = 0 \quad , \quad \xi = 1 \qquad (2.21)
$$

For the partial differential equation (PDV) no analytical solution is possible. This equation can be rewritten as a convection-diffusion equation, in which we scale the velocity with the mean velocity and the time with the period time. The dimensionless velocity is given by $\hat{w}$, the dimensionless time by τ. We obtain the following equation:

$$
\xi\frac{\partial \hat{w}}{\partial \tau} + \chi(\xi,\tau)\frac{\partial \hat{w}}{\partial \xi} - \psi(\tau)\xi\frac{\partial^2 \hat{w}}{\partial \xi^2} = \xi f(\tau), \qquad (2.22)
$$

with $\quad \chi(\xi,\tau) = -\dfrac{\nu T}{R^2(\tau)} + \dfrac{\xi^2}{R(\tau)}\dfrac{dR(\tau)}{d\tau}$, $\quad \psi(\tau) = \dfrac{\nu T}{R^2(\tau)}$ and $f(\tau) = -\dfrac{T}{\rho V}\dfrac{\partial P}{\partial z}(\tau)$.

In the coefficients are the experimentally determined mean and first harmonic of the inner radius substituted, so χ and ψ are determined. The PDV was multiplied with ξ to eliminate the discontinuity for $\xi = 0$. This equation is discretized using a Crank-Nicolson finite differential scheme (Fletcher (1991)):

16

$$\xi_m \frac{\dot{w}_m^{n+1} - \dot{w}_m^n}{\Delta\tau} + \frac{1}{2}\chi_m^n \frac{\dot{w}_{m+1}^n - \dot{w}_{m-1}^n}{2\Delta\xi} +$$

$$+ \frac{1}{2}\chi_m^{n+1} \frac{\dot{w}_{m+1}^{n+1} - \dot{w}_{m-1}^{n+1}}{2\Delta\xi} - \frac{1}{2}\xi_m\psi^n \frac{\dot{w}_{m+1}^n - 2\dot{w}_m^n + \dot{w}_{m-1}^n}{(\Delta\xi)^2} + \qquad (2.23)$$

$$- \frac{1}{2}\xi_m\psi^{n+1} \frac{\dot{w}_{m+1}^{n+1} - 2\dot{w}_m^{n+1} + \dot{w}_{m-1}^{n+1}}{(\Delta\xi)^2} = f^{n+\frac{1}{2}}\xi_m$$

The lower index (m) represents the spatial discretization, the upper index (n) represents the time discretization. This discretization scheme has a second order accuracy in space and time. The Neumann boundary condition is discretized with a forward Euler scheme, which makes the accuracy of the discretization method linear in space and second order in time discretization.

The velocity is solved with a set of matrices for the coefficients of (2.23) accounting for the boundary conditions. The starting velocity profile is the scaled starting velocity profile which is found with the analytical model and further the next eigth cycles are calculated, so the start-effects are damped. There are 11 equidistant space nodes (for half of the cross-section) and 200 time nodes per cycle. The velocity is made dimensionfull again with the mean velocity. Because the velocity profile is axi-symmetric, the profile is mirrored.

The pressure gradient (source term f in (2.22)) is unknown. First we start calculating the velocity profile with the pressure gradient which is found from the analytical model. The adjustment of the pressure gradient per time node is performed iteratively based on the ratio between the experimentally determined flow and the flow determined from the numerical velocity profile (Q_{exp}/Q_{model}; see figure 2.7). This adjusting procedure is carried out until the model flow deviates maximally 0.5% of the experimental flow.
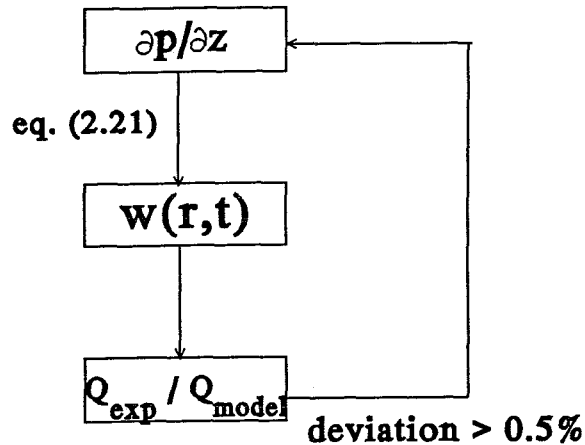

figure 2.7: adjusting of the pressure gradient in order to achieve a flow equal to the experimental flow.

This procedure provides an axial velocity profile with the same flow as the experimental flow. This way the numerical model has the same experimental input parameters as the analytical model (the flow and the inner wall movement). From the numerical and analytical profiles the wall shear rate can be approximated by the finite difference quotient of the axial velocity at the wall. For this the velocity at the node

17

nearest to the wall is divided by the spatial discretization distance (because the velocity at the wall is zero). These two values for the wall shear rate are compared with the experimental approximation of the wall shear rate.

3 Results

3.1 The experiments

3.1.1 Tube deformation

For the instationary flow with α = 4.9 ± 0.1 and *Re* varying harmonically between 200 (± 23) and 800 (± 29) the deformation of the distensible tube is determined. The parameters that characterize this deformation are λ_r (the radial expansion, this is the ratio between the outer radius during the expansion and the outer radius in the reference state when there is no flow through the tube), the rotation angle ϕ_{rot} in degrees and the lateral (u_l) and axial (u_z) translation in mm. These parameters are determined during one flowcycle for the three segments (000, 125 and 250) of the tube. The results are given in figure 3.1 a to d.
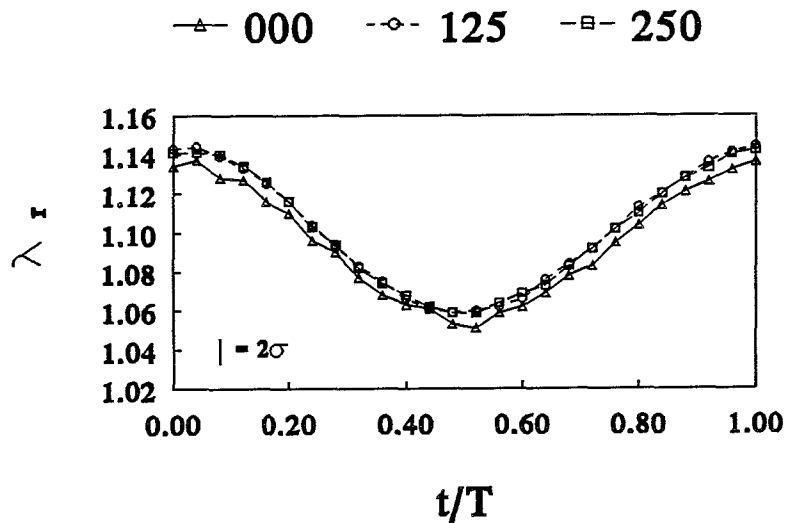
figure 3.1 a: the radial outer expansion against the dimensionless time, determined for the three segments of the tube. σ = 0.007.
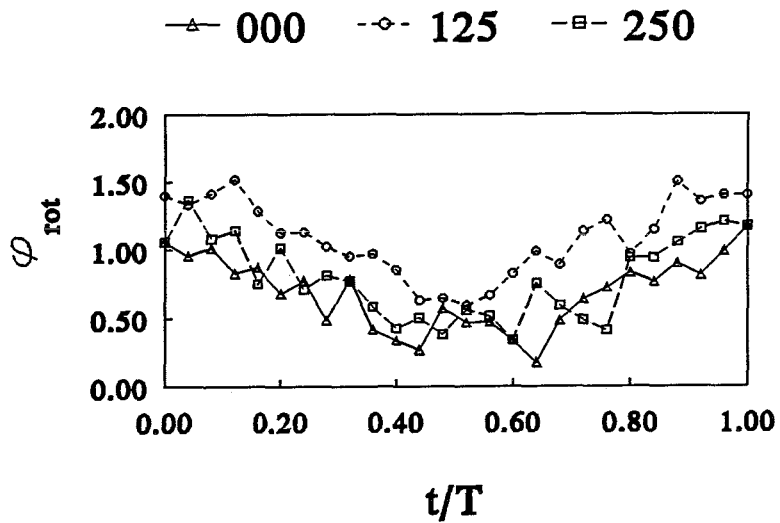
figure 3.1 b: rotation angle (in degrees) against the dimensionless time, determined for the three segments of the tube. The maximal error is 0.3°.
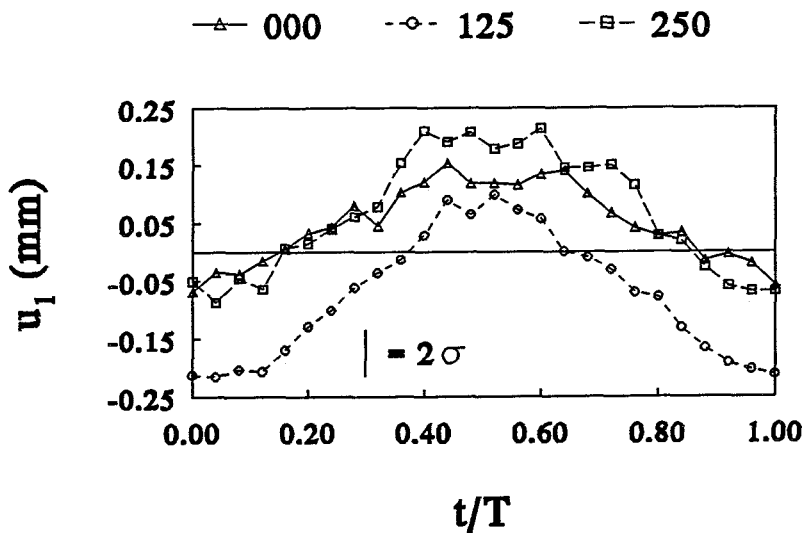

figure 3.1 c: lateral translation (in mm) against the dimensionless time, determined for the three segments of the tube. σ = 0.04 mm.
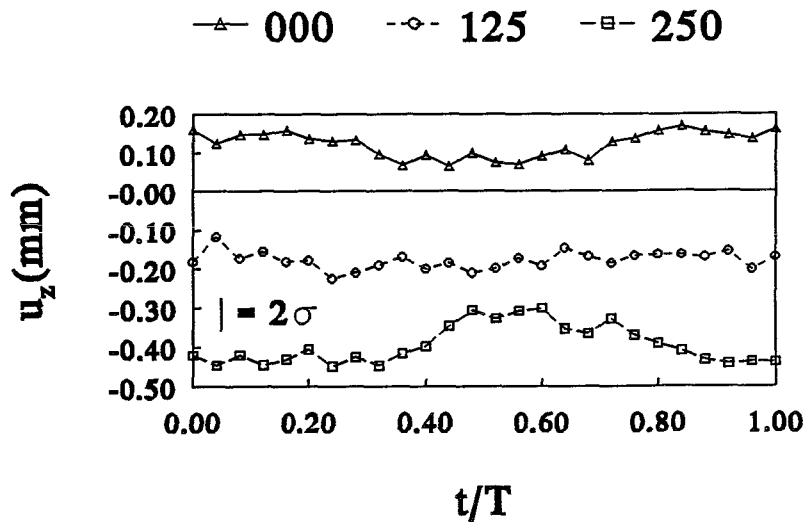
figure 3.1 d: axial translation (in mm) against the dimensionless time, determined for the three segments of the tube. σ = *0.04 mm.*

A positive rotation angle means a rotation counter-clockwise when viewed in the flow direction. A positive lateral translation ($u_l > 0$) means that the segment moves to the left-hand side when viewed in the flow direction. A positive axial translation ($u_z > 0$) means that the segment moves in the flow direction. With these results the axial expansion is not given because this remained at a value of 1 during the whole flowcycle.

From figure 3.1 a to d it can be concluded that the tube undergoes the following deformation during one flowcycle:

- a radial expansion over the whole length of the tube, which varies essentially harmonical between $\lambda_r = 1.14$ and $\lambda_r = 1.06$ with a mean value of 1.10. Between the three segments are no phase differences, so the tube maintains its cylinderical shape.

- a small rotation of the tube (about 1°), which varies slightly with an amplitude of 1°. The value of the rotation angle for the middle segment (125) is slightly bigger than for the two segments closer to the restraints. This middle segment can move more freely than the other two segments.

- a lateral translation of the tube, which varies essentially harmonical. The tube moves from the right-hand side ($u_l < 0$), when the tube is maximally expanded, to the left-hand side ($u_l > 0$). For the middle segment the translation has a different value for the offset than for the two other segments. The amplitude of the translation is for all three segments similar.

- there is no axial translation during the expansion of the tube. The tubewall does undergo an axial translation when the tube is expanded from the reference (no flow) state to the stationary state, when only the stationary pump is active. In this state a stationary flow with $Re = 500$ is generated. During this stationary deformation the segments of the tube are being translated. The outside segments move to the middle of the tube.

21

From figure 3.1 a the movement of the inner radius can be obtained. For this is assumed that the material from which the tube is manufactured (silicon rubber) is incompressible. The results are given in figure 3.2.
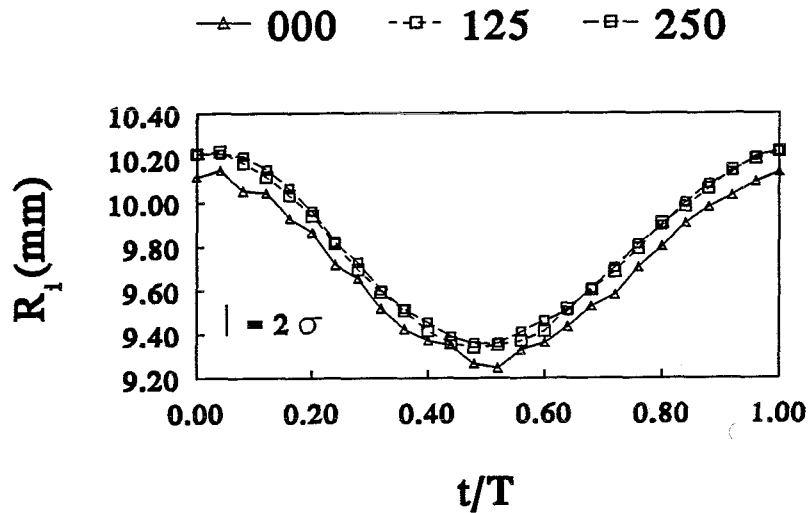

figure 3.2: inner radius (in mm) against the dimensionless time, determined for the three segments of the tube. σ = 0.08 mm.

3.1.2 The transmural pressure

The tube undergoes the deformation as described above as a result of the harmonically varying transmural pressure. This pressure is measured with a cathetertip manometer, which is positioned in the middle of each segment. The value of the transmural pressure inside each segment during one flowcycle is sketched in figure 3.3.
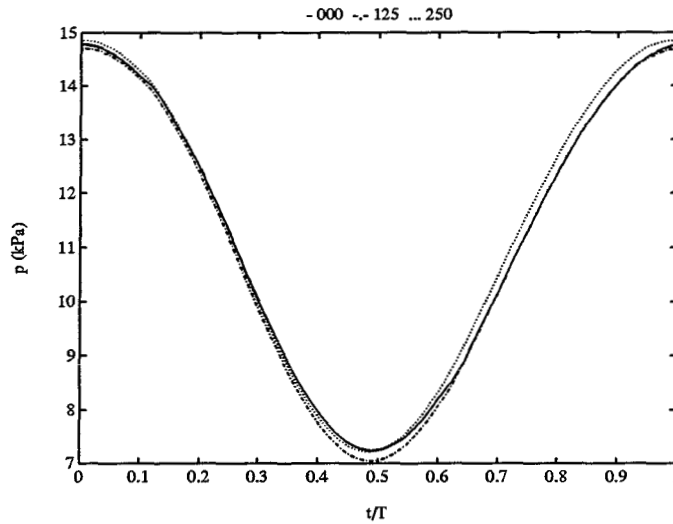
figure 3.3: transmural pressure (in kPa) inside each segment against the dimensionless time. (from Rutten (1993))

From figure 3.3, together with figure 3.1 a, it can be concluded that there is no phase difference between the inner wall movement and the transmural pressure. There are also no phase differences between the transmural pressures inside the three segments, which illustrates the standing wave character pointed out in equations (2.7) and (2.9).

3.1.3 The velocity field

The velocity at each segment is measured along the x- and y-axis (in horizontal and vertical plane). The velocity profiles as measured along the x-axis are shown in figure 3.4 a to c.
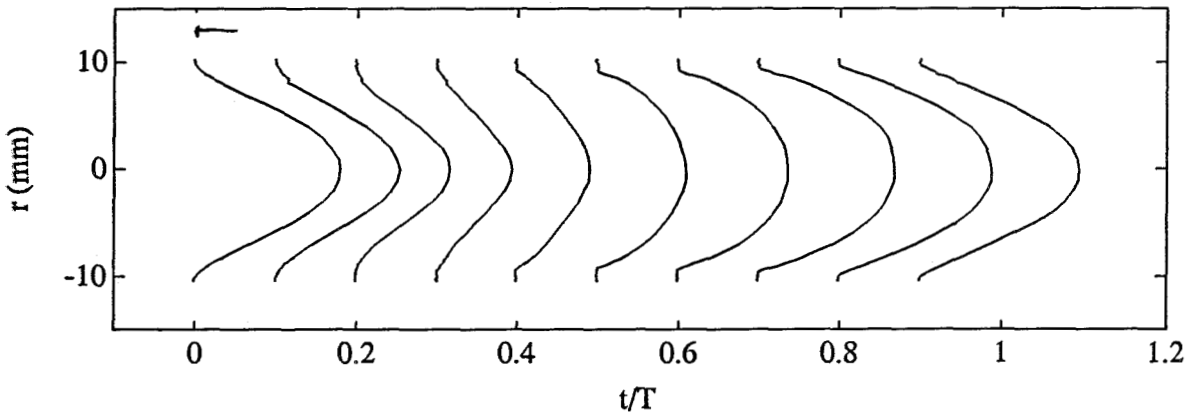

figure 3.4 a: velocity profile measured along the x-axis at segment 000. Accuracy is 3 mm/s. (from Rutten (1993))
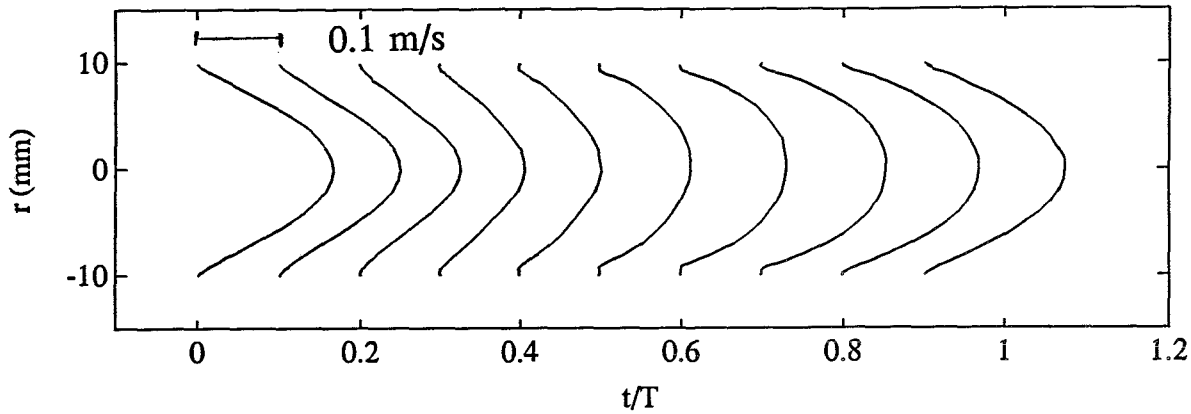
23

figure 3.4 b: velocity profile measured along the x-axis at segment 125. Accuracy is 3 mm/s. (from Rutten (1993))
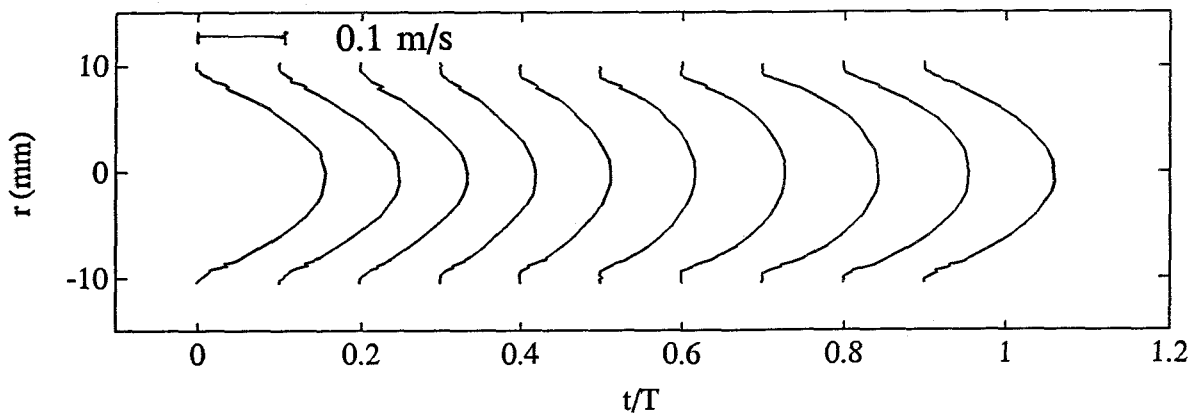

figure 3.4 c: velocity profile measured along the x-axis at segment 250. Accuracy is 3 mm/s. (from Rutten (1993))

Near the wall the ammount of seeding (particles in the fluid which cause the scattering of the laser light and therefore responsible for the velocity signal) is less than near the tube axis, due to lower fluid velocities. This causes noise on the velocity signal near the wall. Comparison of these figures with each other yields the conclusion that the instationary part of the profile decreases in the flow direction. The velocity profiles are also measured along the y-axis. These profiles are not symmetric (Rutten (1993)).

The velocity profile measured along the x-axis is used for the calculation of the local flow. This is done by integrating the velocity profile over the cross-section with the use of the trapezium-rule. For all three segments the local flow is determined. In figure 3.5 these are given, together with the flow measured proximally and distally from the tube during the velocity measurement at segment 000.
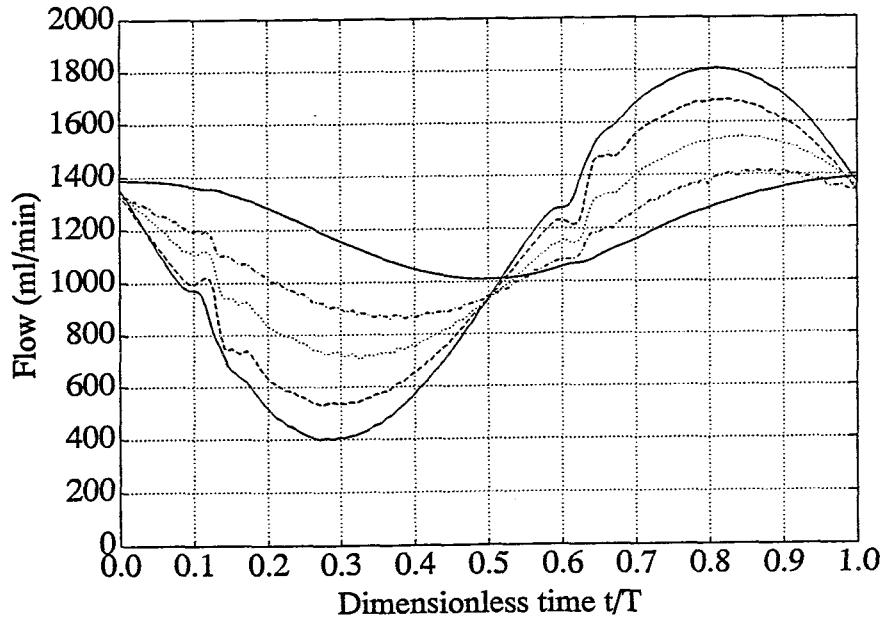
figure 3.5: calculated flow (in ml/min) for all three segments, against the dimensionless time. Also the measured flow proximally and distally from the tube are given. (from Rutten (1993))

A decrease of the amplitude and a phase shift of the flow in the flow direction is found.

The velocity profile measured along the x-axis at segment 000 (figure 3.4 a) is used for comparison with the analytically and numerically predicted velocity profiles. An approximation of the wall shear rate is also obtained from this velocity profile. For this the finite difference quotient is calculated. The difference between two velocity samples near the wall is determined and this is divided by the spatial discretization distance at the wall (= 0.2 mm, see figure 2.6). Difficulty here is to determine whether both samples were taken inside the fluid and thus valid samples, or inside the tube wall. For this the following criterion is used: if the velocity, taken from the sample nearest to the wall is larger than 0 m/s, then the sample is taken inside the fluid.the following wall shear rate, determined at the right-hand side (when viewed in the flow direction) of the velocity profile measured along the x-axis at segment 000, is obtained.
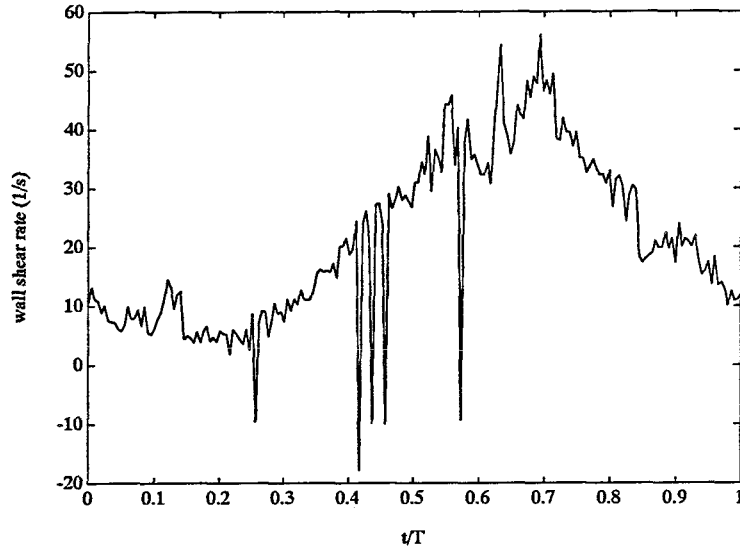
figure 3.6: wall shear rate against the dimensionless time, determined from velocity profiles measured along the x-axis at segment 000 of the tube, with the criterion w > 0 m/s.

This wall shear rate shows some large peaks. Probably some samples are still taken inside the tube wall and not inside the fluid. If the criterion is raised to 0.002 m/s the following wall shear rate is determined.
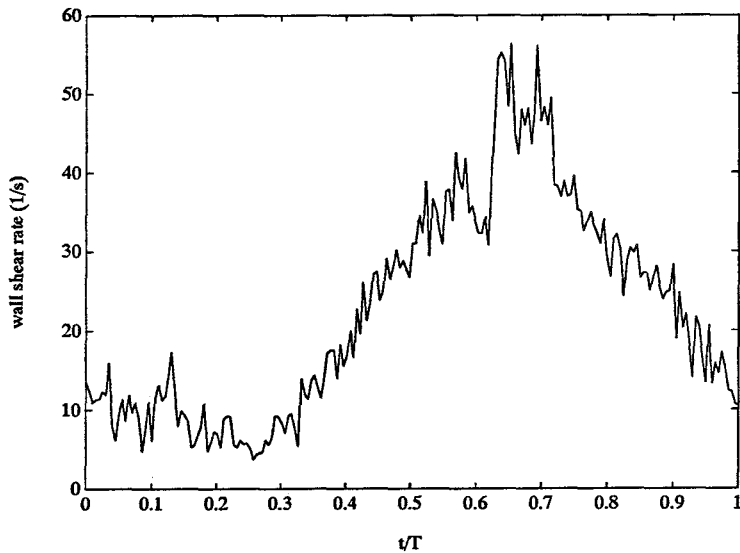

figure 3.7: wall shear rate against the dimensionless time, determined from velocity profiles measured along the x-axis at segment 000 of the tube, with the criterion w > 0.002 m/s.

The wall shear rate shows less noise. The wall shear rate in figure 3.7 is determined on the right-hand side of the tube. The same is done for the wall shear rate on the left-hand side. This way a wall shear rate with a similar course is found, which is not shown.

3.2 The analytical and numerical model

The cross-sectional area and the local flow are both needed as input parameters in the two theoretical models, which predict velocity profiles. The predicted velocity profiles have the same value for the flow as the experimental velocity profile.

The first model is based on Womersley's rigid tube theory. From the local flow and the cross-sectional area an analytical solution for the velocity profile is determined.

The second model is based on Dutta and Tarbell's theory. With the inner radius movement taken into account a numerical solution for the velocity profile is determined with the same value for the flow as the experimental velocity profile. This is obtained by adjusting the pressure gradient.

Both models are used to predict the velocity profile at segment 000. In figure 3.8 both theoretical profiles are given, together with the experimentally determined profile.
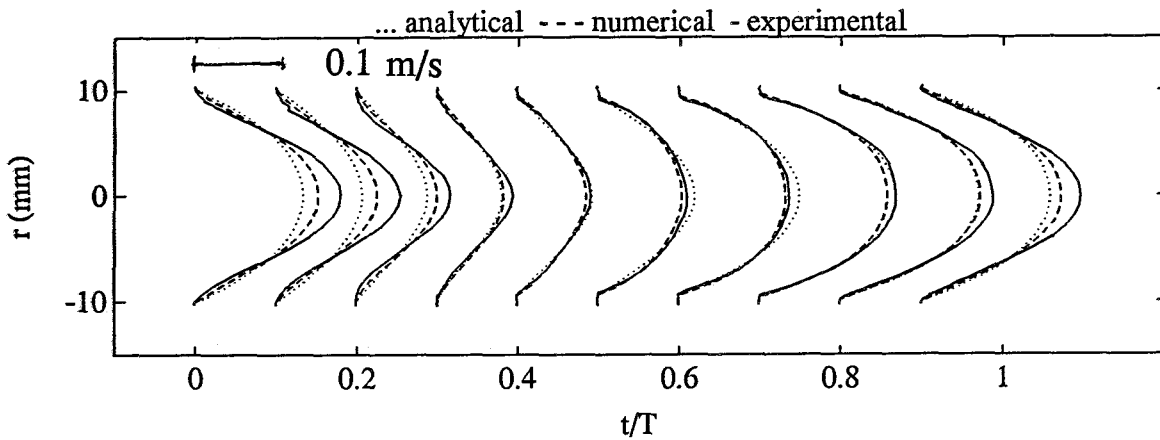

figure 3.8: theoretical velocity profiles for segment 000 together with the experimental profile. The horizontal axis is the dimensionless time, the vertical axis is the position in the tube.

From figure 3.8 it seems that the numerical model leads to a better description of the velocity field than the analytical model. This improvement is going to be quantified in paragraph 4.3.

For both theoretical velocity profiles an axial pressure gradient is used. These gradients are given in figure 3.9 a and b.
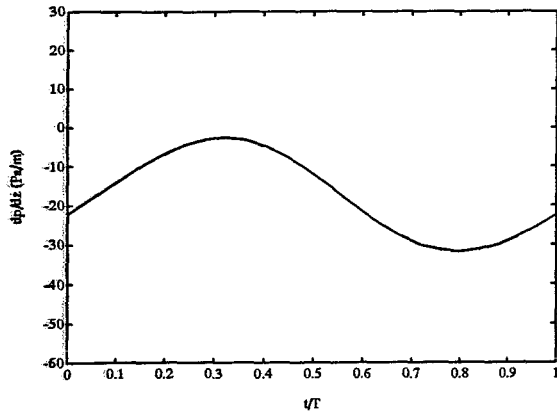
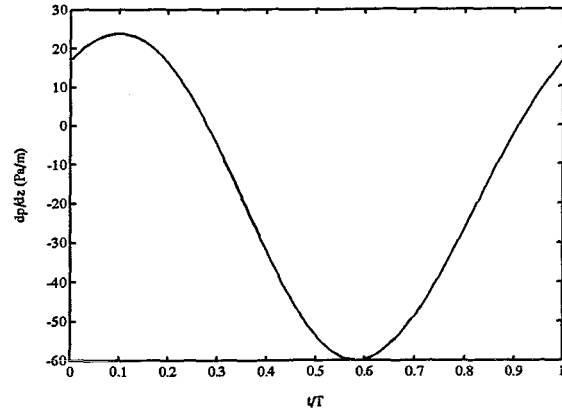figure 3.9 a: the axial pressure gradient, used in the analytical model, against the dimensionless time.

figure 3.9 b: the axial pressure gradient, used in the numerical model, against the dimensionless time.

From figure 3.9 a and b it can be concluded that the axial pressure gradients, used in both models, produce different values for the instationary component (the phase and the amplitude are different). The stationary component (the offset) of the gradients though, leading to the stationary part of the velocity profile, is in both cases almost the same. With the used experimental setup it was not possible to measure the axial pressure gradient. Rutten used a finite element method with moving walls to prescribe the velocity field inside the tube. The pressure gradient is also determined. This gradient oscillates between + 40 Pa/m and -65 Pa/m. The minimal value is reached at $t/T = 0.53$ and the maximal value at $t/T = 1.0$. This also suggests that the numerical model is an improvement to the analytical model.

From the two axial velocity profiles an approximation for the wall shear rate is determined by calculating the finite difference quotient. In figure 3.10 the two wall shear rates are given together with the experimentally determined wall shear rate as it is also shown in figure 3.7. The two theoretical profiles are axisymmetric, so it is trivial to give two gradients for each profile (one at the left-hand side of the tube, one at the right-hand side). For the experimental profile the gradient at the right-hand side of the tube is presented.

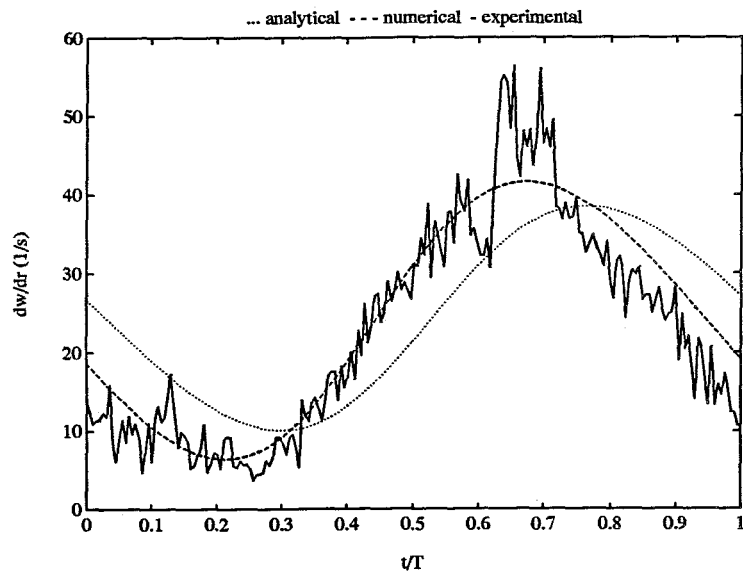The gradient, determined from the numerical profile,

figure 3.10: wall shear rate against the dimensionless time, determined from the two theoretical and the experimental axial velocity profiles for segment 000 of the tube.

shows a better agreement with the experimentally determined gradient than the gradient

28

which is determined from the analytical profile. The mean value (offset) is in both cases almost the same, but the phase and the amplitude of the velocity gradient determined from the analytical profile do not agree with the experimentally determined gradient.

4 Discussion

4.1 Tube deformation

4.1.1 Modeling assumptions

For the experimental setup some modeling assumptions were made. In this paragraph the validity of these assumptions is being investigated.

The material from which the tube is manufactured, is assumed to be isotropic, linearly elastic and the tube is thought to be homogeneous. Dynamic and static experiments with the tube have shown that the material behaves viscoelastic (Appendix B). The viscous part is not really neglible because it can amount to 20% of the elastic part, but in this part of the investigation the viscous damping of the wall is not taken into account.

The human arterial wall is anisotropic, inhomogeneous and behaves non-linearly viscoelastic. The fluid used in the model behaves like an incompressible Newtonian fluid, which is a simplification of the behaviour of blood too. This way conclusions, drawn from the experiments at the model, may not be coupled directly to the in-vivo situation.

Radial homogeneity is a requirement for the rotation detection in the deformation, because the radial expansion is thought to be circumferentially equal. This may lead to a contradiction, because rotation of the tube can occur if the tube is radial inhomogeneous. No attention is paid to this case, because it is not certain where the rotation of the tube finds its origin. Rotation can also occur when the tube is stretched with a small torsion. The rotation is small, although significant.

4.1.2 The deformation

The deformation of the tube is characterized by five parameters: the radial and axial expansion, the rotation angle and the lateral and axial translation. These parameters are determined from the movement of twenty markers on the tube wall. These markers are filmed with a camera which is place above the tube. Each marker is projected on the image-plane (see figure 4.1). By this projection an error in the determination of the true distance (= $R\cos\phi$) between the projection of the marker and the tube axis occurs. This error is called ε in figure 4.1 and for a marker with $\phi = 45°$ ($R\cos\phi = 0.707$ mm) $\varepsilon = 0.018$ mm. The error in the true distance is maximally 2.5%.

figure 4.1: projection of a marker on the image-plane.

From the movement of the markers the expansion, rotation and translation are determined. For the expansion the two dimensional strain field is determined. For each marker individually a Green-Lagrange strain in radial and axial direction is determined, leading to a value for the radial and axial expansion. The expansion of the segment follows, after rotation-correction, from the mean value. This provides a standard deviation too. Inner radius movement is determined from the radial expansion with the assumption that the material from which the tube is manufactured is incompressible. This assumption is valid for silicon rubber.
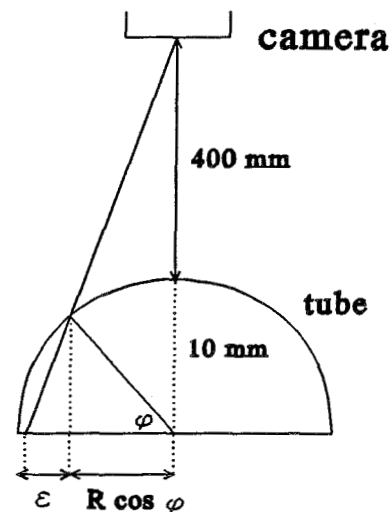
The lateral and axial translation are determined from the centre point movement of the markers.

The three segments of the tube (125 mm apart) move radially in phase. This way the tube maintains its cylindrical shape (figure 3.2).

4.2 Pressure and flow

The radial expansion of the tube is imposed by the transmural pressure. For the experimentally used angular frequency the tube is considered to behave linearly elastic. In this case the transmural pressure and the inner radius movement are in phase, which is also found experimentally.

Between the three segments the transmural pressure is in phase and there is no decrease in amplitude (figure 3.3). The local flow, determined from the measured velocity profiles shows a phase shift and an amplitude decrease in the flow direction (figure 3.5). This can be explained from the wave theory. At the distal end of the tube a variable resistance is placed in the flowcircuit for controlling the transmural pressure and, coupled with this pressure, the inner radius movement. This resistance is a sudden cross-section narrowing. In case a tube is completely closed distally, the reflection coefficient Γ would be 1. For a cross-section narrowing from 18 mm to 2 mm, we may assume that $\Gamma \approx 1$. For both the flow and the pressure standing waves arise inside the tube (as already mentioned in paragraph 2.3, equations (2.6) to (2.10)). At the resistance the flow will be in a node of the wave, while the pressure will be in an antinode.

The three sample points are 125 mm apart. With the tube proportions in respect to the wave length these three sample points are assumed to almost coincide near the node (antinode) of the flow wave (pressure wave). Thus the amplitude of the flow will decrease approximately linear with the distance between the sample points. However, the pressure measured at all three points has the same amplitude at all three points and no phase differences will occur.

With this behaviour in mind a storage model for the flow, which represents the capacitive nature of the tube, is introduced (Appendix D). With this model the flow at an arbitrary position in the tube can be determined without using the velocity profile.

For the local flow the assumption was made that the flow varies harmonical. The flow is established by a stationary and an instationary pump. The stationary pump produces a stationary flow. The instationary flow, produced by the instationary pump, is not quite sinus-shaped, but during the rise and fall of the flow a perturbation occurs (see figure 3.5), due to backlash in the instationary pump. In both theoretical models, which are used to predict the velocity profile, only the offset and the first harmonic of the local flow are taken into account. Higher harmonics are being neglected, although Fast Fourier Transformation of the flow signal shows that the second harmonic has an amplitude of 10% of the amplitude of the first harmonic. The fifth and ninth harmonic each have an amplitude of 3% of the amplitude of the first harmonic. Other harmonics have amplitudes smaller than 1% of the amplitude of the first harmonic.

4.3 The velocity field

In front of the tube a rigid entrance tube of 3.75 m is installed to achieve a fully developed velocity profile at the entrance of the distensible tube. In the horizontale plane a symmetric profile is found (figure 3.4 a to c), but in the verticale plane the profile seemed to be asymmetric. The symmetry did not improve by installing a longer entrance tube. A possible explanation for this asymmetry can be found in the orientation of the flowcircuit

31

with respect of the earth's rotation, but no effort is made to improve the symmetry of the velocity profile by other orientation of the flowcircuit.

From figure 3.4 a to c it can be concluded that the instationary behaviour of the velocity profiles decreases in the flow direction (also illustrated by figure 3.5). The explanation of this behaviour is based on the same arguments that explained the flow behaviour: near the resistance at the distal end of the tube the flow and so the axial velocity decrease almost linear with space due to the standing waveform. At the resistance behind the tube a node for the velocity wave occurs.

Two theoretical models are used to predict the velocity profile at segment 000. First Womersley's theory for the velocity in rigid tubes is applied. Secondly wall motion is taken into account more directly by different treatment of the boundary conditions. This model is derived from Dutta and Tarbell's theory.

In Womersley's model the convective term in the Navier-Stokes equation is neglected. This is allowed for a rigid tube with tube length much longer than the diameter. For distensible tubes a different criterion holds (van de Vosse (1983)):

$$| \frac{\bar{w}}{2c} | \ll 1 \qquad (4.1)$$

With $\bar{w}$ = 0.0852 m/s and c = 6.7 m/s (4.1) is valid. To neglect the second order derivative of the axial velocity component to z the criterion

$$(\frac{R\omega}{2\pi c})^2 \ll 1 \qquad (4.2)$$

must be valid (van de Vosse (1983)). For R = 9 mm and ω = 0.786 rad/s this criterion is valid too. This way (2.13) describes the axial velocity field.

Actually, Womersley's model should only be applied for the flow in rigid tubes. In our experiments though a distensible tube is used with diameter variations of more than 14% occuring. Womersley's theory can not be applied at all means. Womersley also did provide an extension to his theory by introducing wall motion. The boundary conditions (wall motion) are linearized and for a harmonically varying pressure gradient an analytical solution for the flow equation is given, leading to an axial velocity profile. This extension was elaborated for the flow in the distensible tube, but the result did not differ much from the results already obtained from the rigid tube theory. The only real deviation was that the velocity at y = 1 (r = R) is not 0 m/s. Of course the no slip condition has to be met, so this phenomenon is explained with the arising longitudinal wall motion. The tube is longitudinally restrained inside a perspex reservoir (see figure 2.5). This way the extension to the rigid tube theory, as mentioned above, can not be applied to the experimental situation either.

The second model, based on Dutta and Tarbell's theory, took the wall motion directly into account in the boundary conditions. The axial velocity profile is determined from the numerically solved flow equation. A Crank-Nicolson finite difference scheme is used to discretize the flow equation. Both Neumann and Dirichlet boundary conditions are used. The Neumann condition is discretized by a forward Euler scheme. The accuracy of the numerical equation is therefore linear in space and second order in time discretization.

The theoretically predicted velocity profiles have to be compared with the experimentally determined profile. An error definition is used to quantify the differences

32

between two velocity profiles (Rutten (1993)).

The error definition is based on flow rate difference:

$$\varepsilon_Q = \frac{2\pi \int_0^R |V_1 - V_2| r \, dr}{Q} \qquad (4.3)$$

with V_1 and V_2 the velocities that are to be compared, Q the flow (the integrated velocity profile) and R the momentary tube inner radius.

The positions of the sample points for the velocity measurements do not coincide with the nodal points where the velocity in the theoretical models are calculated. They also are time dependent. For the comparison between theoretical and experimental profiles this problem is overcome by fitting the experimental data with orthogonal Legendre polynomials of order 6. The profiles were assumed to be symmetric, so the order had to be even. Also the error between the curvefit and the measured velocity profile had to be minimal. This was achieved for polynomials of order 6. This minimal error, determined with (4.3), amounted to 0.04.

The error definition is used here to compare the two theoretical velocity profiles with the experimentally determined profile. The results are given in figure 4.2.
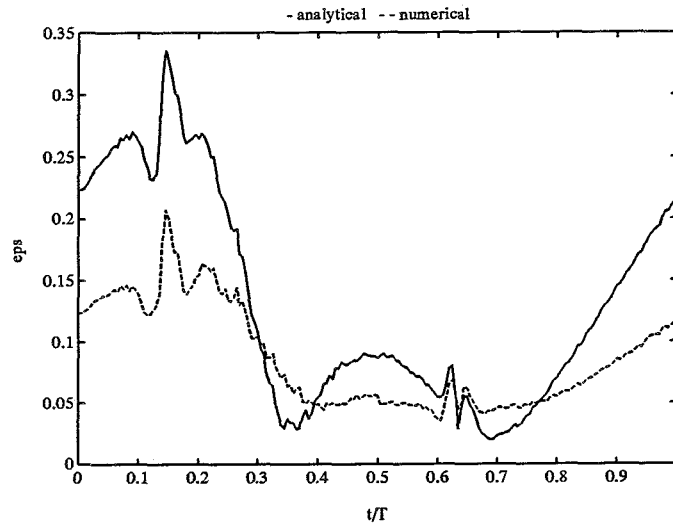

figure 4.2: error (ε_Q = eps) for the analytically and numerically determined profiles against the dimensionless time.

The mean error for the analytically determined profile amounts to 0.13 with a maximum of 0.34. The mean error for the numerically determined profile amounts to 0.09 with a maximum of 0.21. Both curves show peaks at $t/T \approx 0.15$ and 0.65. These peaks are caused by the already mentioned perturbations in the flow, due to backlash in the instationary pump.

Both models seem to fail in describing the flow very well. With this error definition though, it seems that the numerical model is an improvement over Womersley's rigid tube theory.

From the velocity profiles an approximation for the wall shear rate is determined

by calculating the difference quotient at the wall. The reliability of this wall shear rate is coupled to the spatial discretization. The theoretical wall shear rates are determined from the difference between the velocities at two nodes 1 mm apart. Spatial discretization was chosen with CPU time in mind. Smaller discretization implies longer calculation time for the velocity profile.

The experimental wall shear rate is calculated with 0.2 mm spatial discretization and so the accuracy is in order 5 times better than the theoretical wall shear rates. But with the calculation of the experimental wall shear rate another problem arises. Apart from the noise on the wall shear rate due to noise on the velocity signal, another noise source exists in the uncertainty that both velocity samples are taken inside the fluid and not inside the wall. This uncertainty is illustrated by figure 3.6 and figure 3.7. This phenomenon introduces peaks on the wall shear rate. These peaks are eliminated by using a criterion for the minimal value of the velocity. This way an uncertainty is introduced though, because it is unclear whether the wall shear rate is calculated from the velocities nearest to the wall.

When the two theoretical wall shear rates are compared to the experimentally determined value, an improvement in the determination of the wall shear rate with the numerical model in comparison with the wall shear rate following from Womersley's rigid tube theory is found.

4.4 Physiological application

As already mentioned, the experimental model is a great simplification of the in-vivo situation. Therefore the results and conclusions drawn from the experiments may not be coupled directly to the flow in the human communis. Only qualitatively these results may be used for interpretation of the in-vivo flow.

Velocity measurement in human arteries is based on an ultrasound principle. This method provides the velocity on the axis accurately, but flow near the wall can not be detected well.

The numerical model is also applied to determine the axial velocity profile from the velocity value on the tube axis. Instead of adjusting the pressure gradient by the flow ratio, the gradient is adjusted by the ratio between the velocities (experimental and numerical) on the axis. With the used procedure (see paragraph 2.4 and figure 2.7) this does not succeed. Between the velocity on the tube axis and the pressure gradient a phase difference of -90° exists (equation (2.16)), while the phase difference between the flow and the pressure gradient equals -71° (from equation (2.18) together with (2.16)). Apparently, the adjusting parameter (the pressure gradient) may not be completely out of phase with the output parameter (flow and velocity on the tube axis, respectively) for the procedure to succeed. Perhaps a different adjusting procedure will lead to a succesful application of the numerical model.

5 Conclusions

In this study an experimental method for measuring the deformation of a straight, distensible tube is presented. An instationary, harmonical flow through the tube is created, leading to a harmonical varying transmural pressure. This pressure causes radial expansion, rotation and translation of the tube.

Inside the tube a standing wave form for the pressure and the flow is created. Because the tube length is much smaller than the wave length, the pressure inside the tube is the same at all positions, while for the flow the amplitude decreases in the flow direction and a phase shift occurs. For the pressure wave this means that the positions are near the antinode of the wave, for the flow they are near the node.

For the prediction of the fluid velocity two models are used. First Womersley's rigid tube theory does not describe the axial velocity profile very well. The mean error, based on an integral criterion, seems to be 0.13 with a maximal value of 0.34. A second model takes the wall motion directly into account in the boundary conditions. With this model a mean error of 0.09 with a maximal value of 0.21 is found. This still is relatively high, but the model seems to be an improvement on Womersley's theory.

This can also be concluded from the wall shear rate, which is determined with both models. The wall shear rate leading from the second model seems to follow the experimentally determined wall shear rate better than the one leading from Womersley's model.

5.1 Continuation

In this study the deformation of and the flow through a straight, distensible tube is investigated within the "Atherosclerose"-project. The conclusions drawn from this study may not be applied directly to the flow in the human carotid bifurcation. In order to do this, experiments with a model of the bifurcation have to be executed. The experimental method used in this stadium is only usable for the deformation detection of a cylindrical segment, but the method can be adjusted for other geometries.

Also a more realistic flow has to be applied through the model to account for the flow through the human carotid bifurcation. Blood and human arterial wall can be modelled by using another fluid and material for the tube. The choice of these is complicated by the velocity measurement. In the experiments the velocity measurement is based on LDA, which means that the tube has to be transparant and the refraction index of the fluid has to be matched with the refraction index of the tube material. So either the same material and fluid have to be used (or material which is comparable) or a different velocity measurement method, like ultrasound, has to be used. The deformation detection does not impose conditions on the fluid and tube material.

Thusfar the rotation is determined from a minimal residu method in the radial expansion. However, the rotation can be determined experimentally using two cameras which film the tube segments in two orthogonal views. Also the translation of the whole tube can be determined this way.

References

[1]   Balasubramanian, K.
        An experimental investigation of steady flow at an arterial bifurcation
        thesis, Georgia Institute of Technology, Atlanta, 1979

[2]   Bharadvaj, B.K., Mabon, R.F. Giddens, D.P.
        Steady flow in the human carotid bifurcation. Part 1: flow visualization
        Journal of Biomechanics, Volume 15, p 349-362, 1982

[3]   Dutta, A., Tarbell, J.M.
        Numerical simulation of sinusoidal flow in a straight elastic tube: effects of phase
        angles
        Biorheology, Volume 26, p 1-22, 1989

[4]   Fletcher, C.A.J.
        Computational techniques for fluid dynamics.
        Volume 1: Fundamental and general techniques
        Second edition, p 299-316, Springer-Verlag, Berlin, 1991

[5]   Paterson, A.R.
        A first course in fluid dynamics
        First edition, p 127-138, Cambridge University Press, Cambridge, 1983

[6]   Pedley, T.J.
        The fluid dynamics of large blood vessels
        Cambridge University Press, Cambridge, 1980

[7]   Reuderink, P.J.
        Analysis of the flow in a 3D distensible model of the carotid artery bifurcation
        Ph.D-thesis, Eindhoven 1991

[8]   Rutten, M.C.M.
        Experimental and numerical analysis of instationary flow through a straight
        distensible tube
        Master-thesis, WFW 93-066, Eindhoven 1993

[9]   van de Vosse, F.N.
        Gedrag van stromingen veroorzaakt door een harmonische drukgradiënt in starre en
        elastische buizen
        report Eindhoven University of Technology WFW, p 12-13, 1983

[10]   Vossers, G.
        Fysische transportverschijnselen voor W
        Syllabus Eindhoven University of Technology, p 99-101, Eindhoven, 1986

[11] Womersley, J.R.
An elastic tube theory of pulse transmission and oscillatory flow in mammalian arteries
Technical report WADC-TR 56-614, Wright Air Development Centre, 1957

Appendix A: Detection of the tube rotattion

The radial expansion of a segment is measured from the movement of twenty markers. These are placed on the outside wall of the tube on four parallel virtual lines (five markers per line). These lines have a length of 32 mm and are parallel to the tube axis. Expansion is determined from the two dimensional strain field. This strain field is calculated from the movement of each marker with regard to the surrounding markers after the translation of the whole segment is calculated. The calculated radial expansion at segment 250, given in figure A.1, is the expansion from the central marker of each line, with line 1 corresponding to the line closest to the right side of the tube, when viewed in the flow direction. The other line numbers (2, 3 and 4) are arranged with increasing angular difference to line 1.
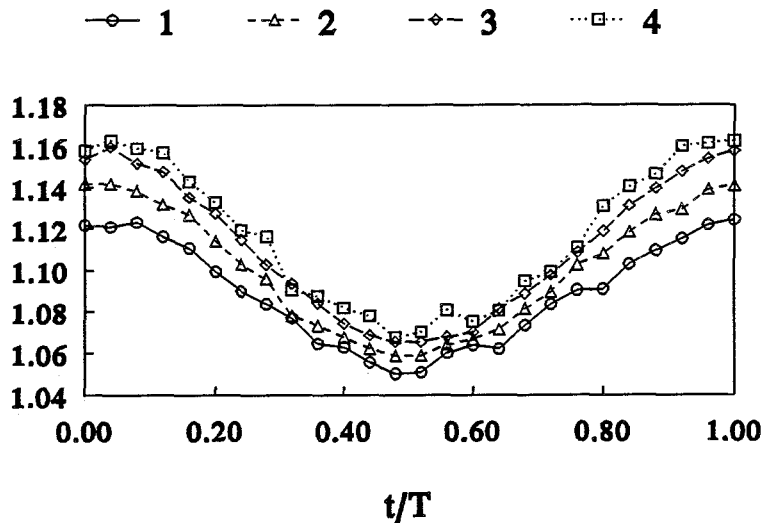
figure A.1: radial expansion of each line of segment 250 before rotation correction, against the dimensionless time.

Because the radial expansion of the tube seems to depend on the circumferential position of a marker, as shown in figure A.1, the following consideration of the movement of the segment is made. When the tube is considered to be circumferentially homogeneous, the radial expansion of a marker on each line has to be equal. Therefore an extra movement of markers together with the radial expansion and translation occurs.

This extra movement is a rigid rotation of the segment. During the maximum in the radial expansion the segment is rotated to the left side of the tube. This way the amplitude of the movement of a marker as projected on the image plane, closer to the left side is bigger than the amplitude of the movement of other markers. This results in a bigger value for the radial expansion.

After the circumferential position of each marker in the reference state is determined, the total movement of the cluster of markers is corrected for this rotation. This is done in an iterative way, with minimal residu for the radial expansion. From this residu

the standard deviation is calculated.

In figure A.2 the radial expansion of segment 250 for the central marker of each line is given again, but now after rotation correction. This way the radial expansion of each markers does not differ systematically.
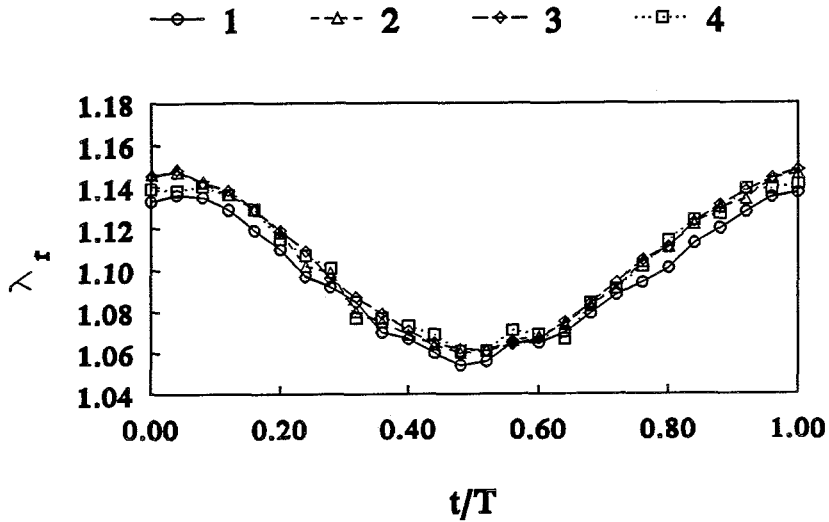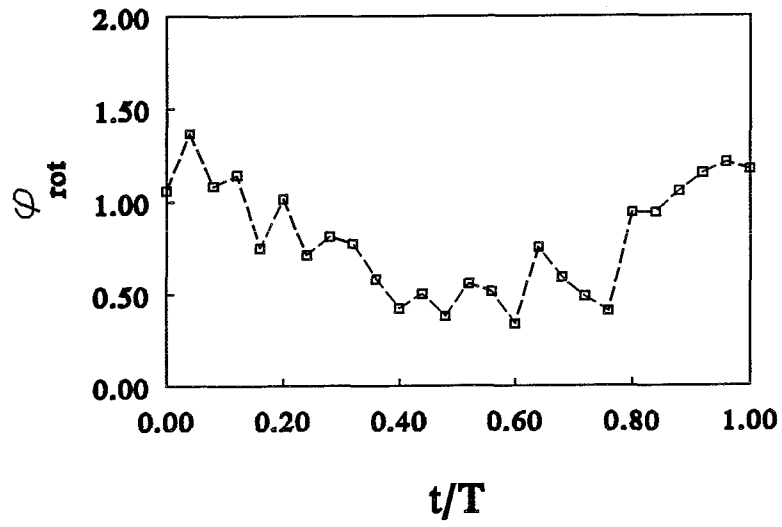

figure A.2: radial expansion of each line of segment 250 after rotation correction, against the dimensionless time.

In figure A.3 the rotation angle is given.

figure A.3: rotation angle (in deg) against the dimensionless time, determined at segment 250.

Appendix B: Results of the deformation measurement

First static deformation of the tube is measured. This is done by setting the stationary pump at different values. The instationary pump is switched off. The radial expansion is determined from the movement of the markers. Also the radial expansion is determined from the direct measured outer radius. This is done by traversing the laser from the upperside of the tube to the lowerside and measuring the outer diameter. In figure B.1.a the radial expansion is given. The optical measured expansion is indicated with t, the direct measured expansion is indicated with l. Deformation is measured at segment 000 (0), 125 (1) and 250 (2).
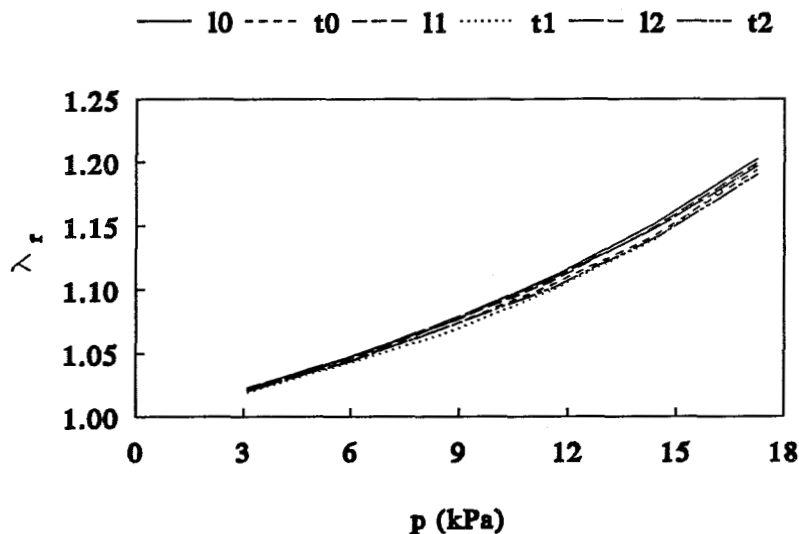
figure B.1.a: radial expansion against the transmural pressure (in kPa), determined from two methods.

In the following figures the rotation and translation are given.
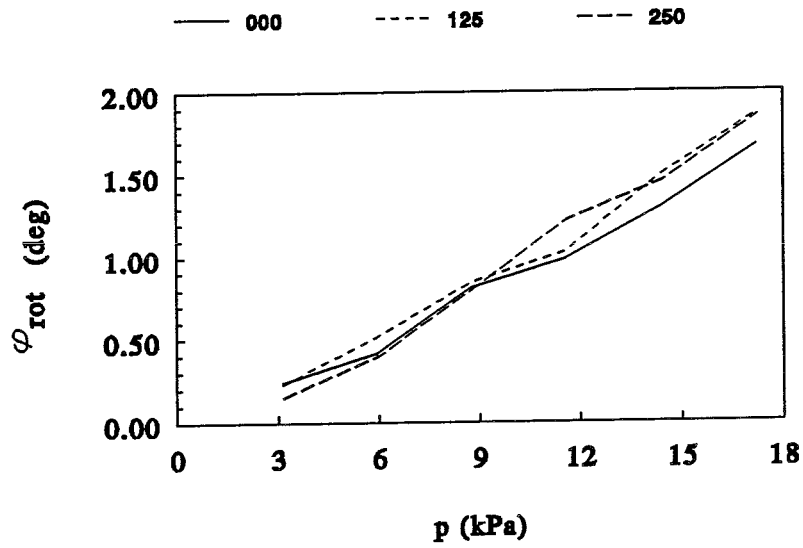
figure B.1.b: rotation angle (in deg) against the transmural pressure (in kPa).
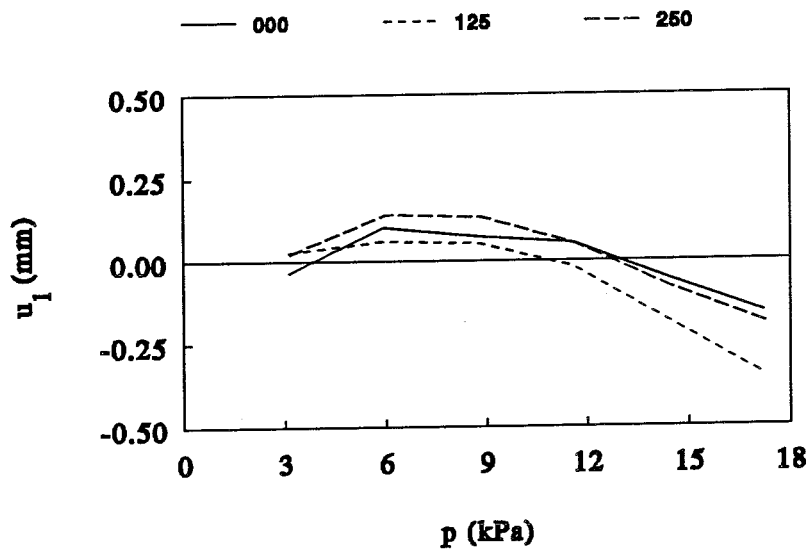

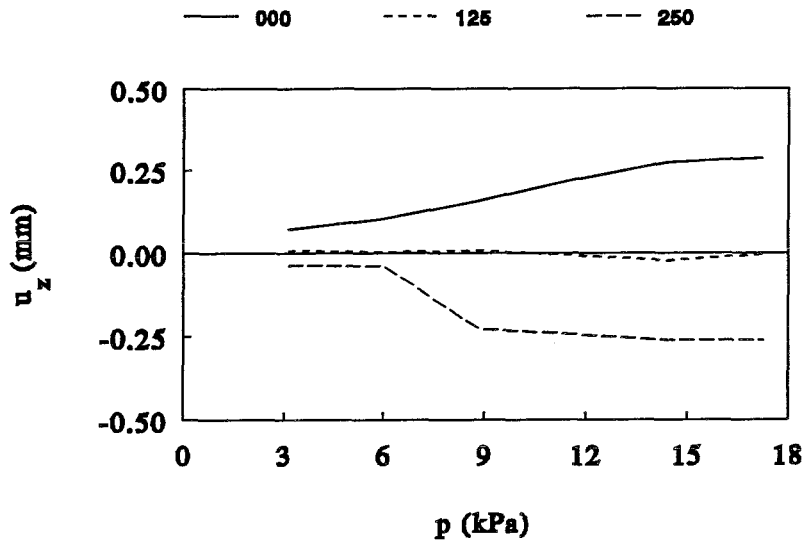*figure B.1.c: lateral translation (in mm) against the transmural pressure (in kPa).*

figure B.1.d: axial translation (in mm) against the transmural pressure (in kPa).

From the radial expansion the modulus of elasticity is calculated with the assumption that the tube material is incompressible. In figure B.2.a this is done from the static measured expansion. In figure B.2.b this is done from the dynamic measured expansion as it was given in figure 3.1.a. The static determined modulus is not a constant value, but increases with increasing transmural pressure. This static determined modulus is about 20% higher than the dynamic determined modulus. The mean value of the dynamic determined modulus is $0.99 \cdot 10^6$ N/m^2. The standard deviation is $0.03 \cdot 10^6$ N/m^2.

In figure B.3.a and b the distensibility of the tube is given. They are determined from the cross-section - transmural pressure relation. For this relation a second order polynomial is taken. The distensibility is in both cases (static and dynamic) not a constant value.
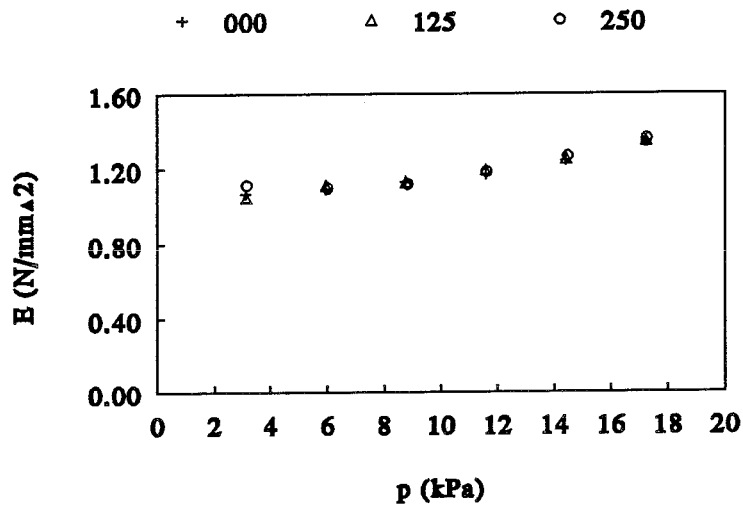
figure B.2.a: modulus of elasticity (in N/mm²) against the transmural pressure (in kPa). This is determined from the static experiments.
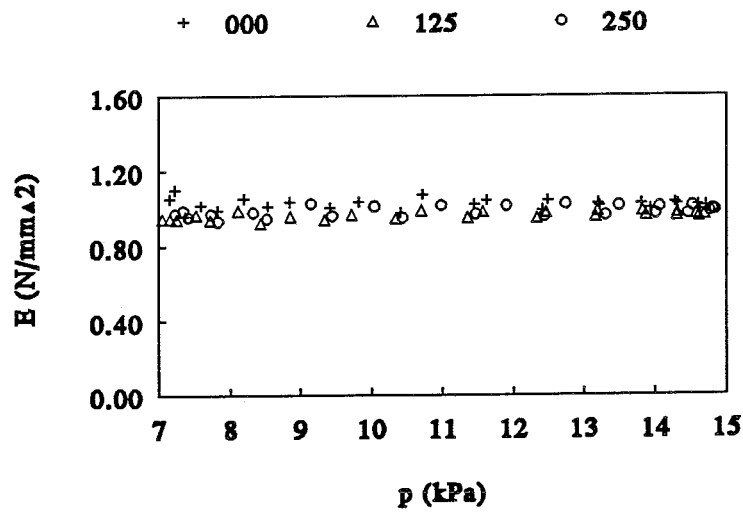

figure B.2.b: modulus of elasticity (in N/mm²) against the transmural pressure (in kPa). This is determined from the dynamic experiments.
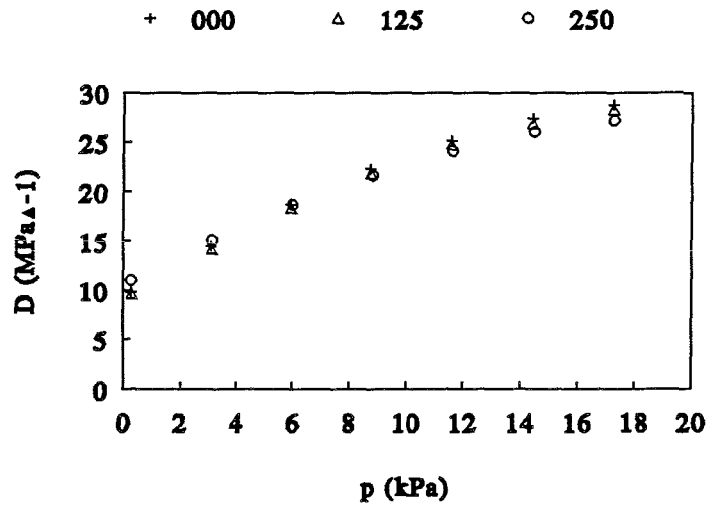
44

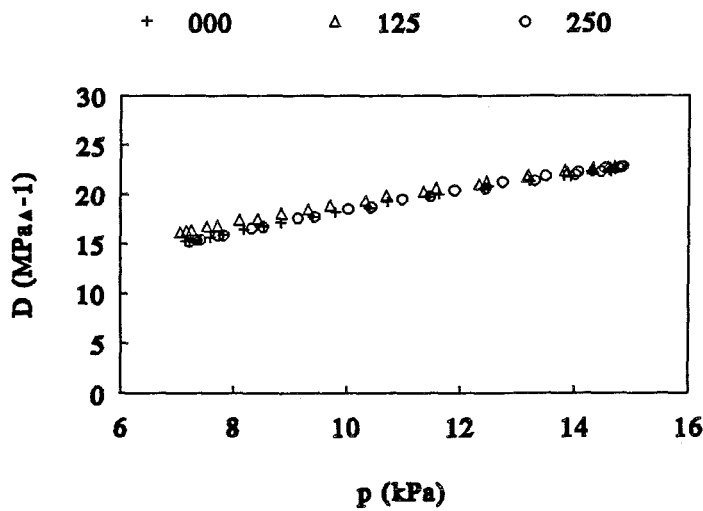*figure B.3.a: distensibility D (in MPa^{-1}) against the transmural pressure (in kPa). This is determined from the static experiments.*

figure B.3.b: distensibility D (in MPa^{-1}) against the transmural pressure (in kPa). This is determined from the dynamic experiments.

The effect of the restainted ends to the radial expansion is also investigated with a static experiment. The outer diameter at 13 axial sample positions near the restainted end where the flow enters the tube is determined as function of the transmural pressure. The sample positions are at 2.5, 3.5, 4.5, 5.5, 6.5, 7.5, 9.5, 11.5, 13.5, 15.5, 17.5, 19.5 and 21.5 mm of the restainted end. The outer diameter is measured with the laser. The results are given in figure B.4 where for 8 values of the transmural pressure the outer diameter at these sample points is given. The sample positions are identified with the distance of each position to segment 000. Therefore the sample position at 2.5 mm of the restainted end becomes sample point -104 and the position at 21.5 mm becoms point -85.
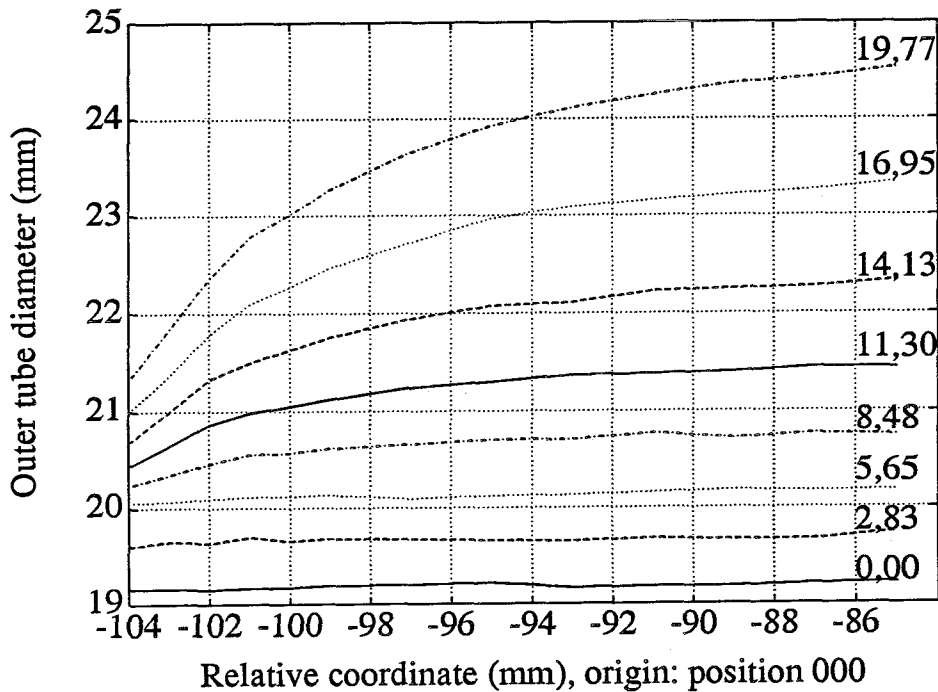

figure B.4: outer diameter (in mm) of the tube against the axial position, at 8 different values for the transmural pressure (in kPa).

From this it can be concluded, that the tube expands almost cylindrical when measured 11.5 mm from the restainted end; at sample points further than 11.5 mm from these ends the effect of the restainted ends can be ignored.

Appendix C: Radial coordinate transformation of the axial component of the Navier-Stokes equation

The axial component of the Navier-Stokes equation is

$$\frac{\partial w}{\partial t} + u\frac{\partial w}{\partial r} + w\frac{\partial w}{\partial z} = -\frac{1}{\rho}\frac{\partial p}{\partial z} + \nu[\frac{\partial^2 w}{\partial r^2} + \frac{1}{r}\frac{\partial w}{\partial r} + \frac{\partial^2 w}{\partial z^2}] \qquad (C.1)$$

Wall movement is taken into account by the radial coordinate transformation $\xi = \dfrac{r}{R(t,z)}$

which means we have to transform (C.1) from the $w(r,t,z)$ domain to the $w(\xi,t,z)$ domain. We do this by invoking the relations

$$dw = (\frac{\partial w}{\partial t})_{r,z}dt + (\frac{\partial w}{\partial r})_{z,t}dr + (\frac{\partial w}{\partial z})_{t,r}dz \qquad (C.2)$$

$$dw = (\frac{\partial w}{\partial t})_{\xi,z}dt + (\frac{\partial w}{\partial \xi})_{z,t}d\xi + (\frac{\partial w}{\partial z})_{t,\xi}dz \qquad (C.3)$$

The indices show which variables are held at a constant value during the partial derivative. Since $\xi = \xi(r,t,z)$

$$d\xi = (\frac{\partial \xi}{\partial t})_{r,z}dt + (\frac{\partial \xi}{\partial r})_{z,t}dr + (\frac{\partial \xi}{\partial z})_{t,r}dz \qquad (C.4)$$

Combining (C.4) to (C.3) yields

$$dw = (\frac{\partial w}{\partial t})_{\xi,z}dt + (\frac{\partial w}{\partial \xi})_{z,t}[(\frac{\partial \xi}{\partial t})_{r,z}dt + (\frac{\partial \xi}{\partial r})_{z,t}dr + (\frac{\partial \xi}{\partial z})_{t,r}dz] + (\frac{\partial w}{\partial z})_{t,\xi}dz \quad (C.5)$$

or

$$dw = [(\frac{\partial w}{\partial t})_{\xi,z} + (\frac{\partial w}{\partial \xi})_{z,t}(\frac{\partial \xi}{\partial t})_{r,z}]dt + (\frac{\partial w}{\partial \xi})_{z,t}(\frac{\partial \xi}{\partial r})_{z,t}dr +$$
$$+ [(\frac{\partial w}{\partial \xi})_{z,t}(\frac{\partial \xi}{\partial z})_{t,r} + (\frac{\partial w}{\partial z})_{t,\xi}]dz \qquad (C.6)$$

Comparing (C.6) to (C.2) leads to the following equations:

$$(\frac{\partial w}{\partial t})_{r,z} = (\frac{\partial w}{\partial t})_{\xi,z} + (\frac{\partial w}{\partial \xi})_{z,t}(\frac{\partial \xi}{\partial t})_{r,z} \qquad (C.7)$$

$$(\frac{\partial w}{\partial r})_{z,t} = (\frac{\partial w}{\partial \xi})_{z,t}(\frac{\partial \xi}{\partial r})_{z,t} \qquad (C.8)$$

47

$$\left(\frac{\partial w}{\partial z}\right)_{t,r} = \left(\frac{\partial w}{\partial \xi}\right)_{z,t}\left(\frac{\partial \xi}{\partial z}\right)_{t,r} + \left(\frac{\partial w}{\partial z}\right)_{t,\xi} \tag{C.9}$$

Now

$$\frac{\partial}{\partial r}\left[\left(\frac{\partial w}{\partial r}\right)_{z,t}\right]_{z,t} = \frac{\partial}{\partial r}\left[\left(\frac{\partial w}{\partial \xi}\right)_{z,t}\left(\frac{\partial \xi}{\partial r}\right)_{z,t}\right]_{z,t} \tag{C.10}$$

or

$$\left(\frac{\partial^2 w}{\partial r^2}\right)_{z,t} = \left(\frac{\partial w}{\partial \xi}\right)_{z,t}\left(\frac{\partial^2 \xi}{\partial r^2}\right)_{z,t} + \left(\frac{\partial^2 w}{\partial \xi^2}\right)_{z,t}\left(\frac{\partial \xi}{\partial r}\right)_{z,t}^2 \tag{C.11}$$

Also,

$$\frac{\partial}{\partial z}\left[\left(\frac{\partial w}{\partial z}\right)_{t,r}\right]_{t,r} = \frac{\partial}{\partial z}\left[\left(\frac{\partial w}{\partial \xi}\right)_{z,t}\left(\frac{\partial \xi}{\partial z}\right)_{t,r} + \left(\frac{\partial w}{\partial z}\right)_{t,\xi}\right]_{t,r} \tag{C.12}$$

or

$$\begin{aligned}
\left(\frac{\partial^2 w}{\partial z^2}\right)_{t,r} &= \left(\frac{\partial w}{\partial \xi}\right)_{z,t}\left(\frac{\partial^2 \xi}{\partial z^2}\right)_{t,r} + \left(\frac{\partial^2 w}{\partial z^2}\right)_{t,\xi} + \left(\frac{\partial^2 w}{\partial \xi^2}\right)_{z,t}\left(\frac{\partial \xi}{\partial z}\right)_{t,r}^2 + \\
&\quad + \left(\frac{\partial w}{\partial \xi}\right)_{z,t}\frac{\partial}{\partial \xi}\left[\left(\frac{\partial \xi}{\partial z}\right)_{t,r}\right]_{z,t}\left(\frac{\partial \xi}{\partial z}\right)_{t,r} + \left(\frac{\partial^2 w}{\partial \xi \partial z}\right)_{t}\left(\frac{\partial \xi}{\partial z}\right)_{t,r}
\end{aligned} \tag{C.13}$$

With the already mentioned radial transformation we can derive

$$\left(\frac{\partial \xi}{\partial r}\right)_{z,t} = \frac{1}{R} \tag{C.14}$$

$$\left(\frac{\partial^2 \xi}{\partial r^2}\right)_{z,t} = 0 \tag{C.15}$$

$$\left(\frac{\partial \xi}{\partial t}\right)_{r,z} = -\frac{r}{R^2}\left(\frac{\partial R}{\partial t}\right)_z = -\frac{\xi}{R}\left(\frac{\partial R}{\partial t}\right)_z \tag{C.16}$$

$$\left(\frac{\partial \xi}{\partial z}\right)_{t,r} = -\frac{r}{R^2}\left(\frac{\partial R}{\partial z}\right)_t = -\frac{\xi}{R}\left(\frac{\partial R}{\partial z}\right)_t \tag{C.17}$$

$$\frac{\partial}{\partial \xi}\left[\left(\frac{\partial \xi}{\partial z}\right)_{t,r}\right]_{z,t} = -\frac{1}{R}\left(\frac{\partial R}{\partial z}\right)_t \tag{C.18}$$

48

$$\left(\frac{\partial^2 \xi}{\partial z^2}\right)_{t,r} = \frac{2r}{R^3}\left(\frac{\partial R}{\partial z}\right)_t^2 - \frac{r}{R^2}\left(\frac{\partial^2 R}{\partial z^2}\right)_t = \frac{2\xi}{R^2}\left(\frac{\partial R}{\partial z}\right)_t^2 - \frac{\xi}{R}\left(\frac{\partial^2 R}{\partial z^2}\right)_t \qquad (C.19)$$

These equations are substituted in equations (C.7) to (C.13). The resulting terms are substituted in the axial component of the Navier-Stokes equation (C.1). This results in the following equation, where all indices are dropped:

$$\frac{\partial w}{\partial t} - \frac{\xi}{R}\frac{\partial w}{\partial \xi}\frac{\partial R}{\partial t} + \frac{u}{R}\frac{\partial w}{\partial \xi} + w\left[-\frac{\xi}{R}\frac{\partial w}{\partial \xi}\frac{\partial R}{\partial z} + \frac{\partial w}{\partial z}\right] =$$

$$= -\frac{1}{\rho}\frac{\partial p}{\partial z} + \nu\left\{\frac{1}{R^2}\frac{\partial^2 w}{\partial \xi^2} + \frac{1}{\xi R^2}\frac{\partial w}{\partial \xi} + \frac{\partial^2 w}{\partial z^2} + \frac{\partial w}{\partial \xi}\left[\frac{2\xi}{R^2}\left(\frac{\partial R}{\partial z}\right)^2 + \right.\right. \qquad (C.20)$$

$$\left.\left. - \frac{\xi}{R}\frac{\partial^2 R}{\partial z^2}\right] + \frac{\partial^2 w}{\partial \xi^2}\left(-\frac{\xi}{R}\frac{\partial R}{\partial z}\right)^2 + \frac{\partial w}{\partial \xi}\left(-\frac{1}{R}\frac{\partial R}{\partial z}\right)\left(-\frac{\xi}{R}\frac{\partial R}{\partial z}\right) + \frac{\partial^2 w}{\partial \xi \partial z}\left(-\frac{\xi}{R}\frac{\partial R}{\partial z}\right)\right\}$$

This equation is equal to (2.19).

Now an order estimation for this equation is executed. There are 4 terms (expressions between brackets are counted as 1 term) on the left-hand side (l.h.s.) of equation (C.20) and 8 terms on the right-hand side (r.h.s.). For each parameter the following values are used in the estimations:

w : mean axial velocity (= 0.085 m/s)
t : 1/angular frequency (= 0.786 s)
ξ : the maximal value (1).
u : the mean wall velocity (= $2\cdot10^{-4}$ m/s)
R : the mean inner radius (= 9.8 mm)
z : the tube length (= 0.5 m)
ρ : the specific gravity of the fluid (= 1262 kg/m^3)
p : the mean transmural pressure (= 11 kPa)
ν : the kinematic viscosity of the fluid (= $2.5\cdot10^{-6}$ m^2/s)

For each term the following order estimation is found:

l.h.s., term 1 : 0.108   r.h.s., term 1 : -17
l.h.s., term 2 : -0.108   r.h.s., term 2 : 0.002
l.h.s., term 3 : 0.002   r.h.s., term 3 : 0.002
l.h.s., term 4 : 0   r.h.s., term 4 : $8.5\cdot10^{-7}$

If the tube maintains cylindrical during the deformation (R is independent from the axial coordinate z), the terms 5, 6, 7 and 8 on the right hand side are zero.

On the l.h.s. terms 3 and 4 are neglected over terms 1 and 2 and on the r.h.s. terms 4, 5, 6, 7 and 8 are neglected over terms 1, 2 and 3. This leads, after some rewriting, to the following equation:

$$\frac{\partial w}{\partial t} = \nu\left[\frac{1}{R^2}\frac{\partial^2 w}{\partial \xi^2} + \frac{1}{\xi R^2}\frac{\partial w}{\partial \xi}\right] - \frac{1}{\rho}\frac{\partial p}{\partial z} + \frac{\xi}{R}\frac{\partial R}{\partial t}\frac{\partial w}{\partial \xi} \qquad (C.21)$$

This equation is equal to (2.20).

49

Appendix D: Storage model for the flow

If the transmural pressure in a straight, linearly elastic tube occurs as a standing waveform with a wave length much longer than the tube length, the radial expansion at axial positions on the wall near each other will be identical. This way the tube will maintain its cylindrical shape. If the tube expands radially, fluid will be stored and this will be released again when the tube shrinks down. This way the local flow does not depend on the flow at the entrance alone, but also on the wall movement.

For an infinitesimal small segment of the tube (figure D.1) the following model for the flow will be determined.
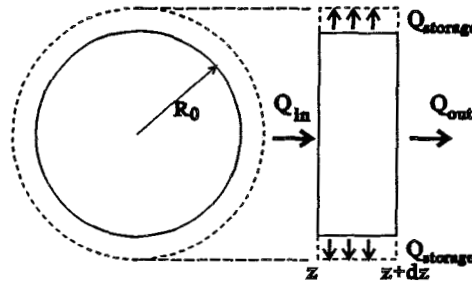

figure D.1: storage model for the flow.

For the outgoing flow holds:

$$Q_{out} = Q_{in} - Q_{storage} \tag{D.1}$$

with for the storage flow for an infinitesimal small segment ·

$$Q_{storage} = u(R_0)2\pi R_0 dz \tag{D.2}$$

with R_0 the tube inner radius in the reference state and $u(R_0)$ the radial fluid velocity at $r = R_0$. In case of small deformations of the tube wall this radial fluid velocity can be approximated by the velocity of the wall movement dR/dt. This way the flow at an axial position z becomes

$$Q(z) = Q_{in} - 2\pi R_0 z \frac{dR}{dt} \tag{D.3}$$

The wall movement becomes, after linearization

$$R = R_0 + \hat{R}\cos(\omega t + \phi_R) \tag{D.4}$$

and (D.3) becomes

50

$$Q(z) = Q_{in} + 2\pi R_0 \hat{R} \omega z \sin(\omega t + \phi_\lambda) \tag{D.5}$$

This way the flow at an arbitrary axial position in the tube can be calculated. This is done for the local flow at segments 125 and 250. For the ingoing flow the local flow at segment 000 is used. Both flows are compared to the flows which are determined by integrating the axial velocity profile over the cross-section. The results are given in the following figure.
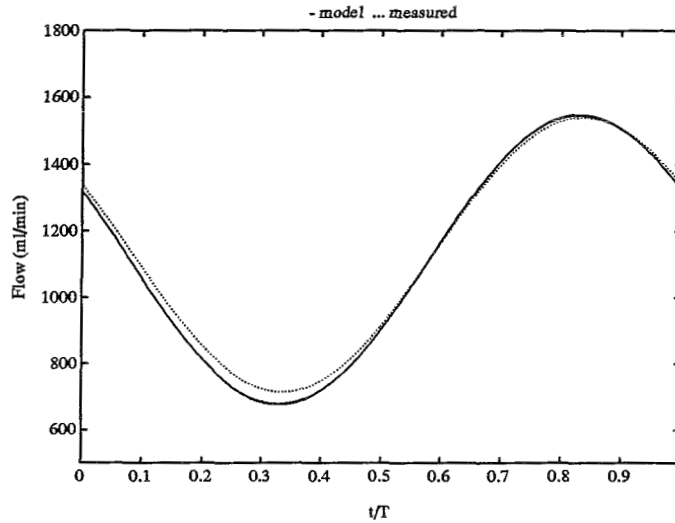

figure D.2a: the experimental determined flow and the flow calculated from the storage model against the dimensionless time at segment 125.
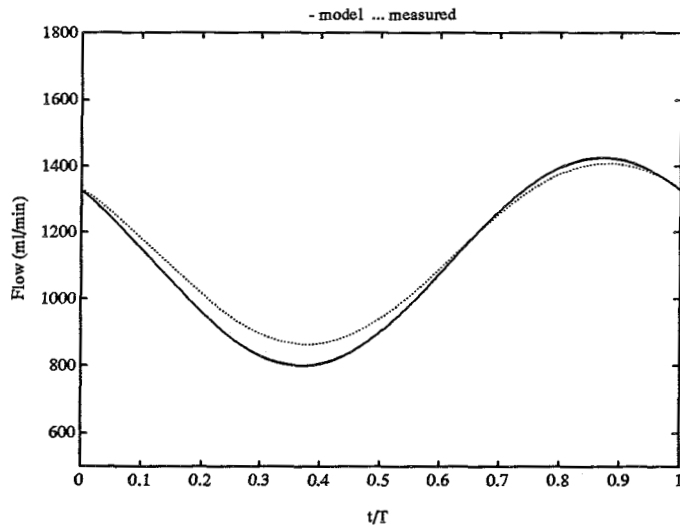

figure D.2b: the experimental determined flow and the flow calculated from the storage model against the dimensionless time at segment 250.

These figures illustrate the validation of the storage model for the flow.